ACSNANO

www.acsnano.org

ARTICLE

# Targeting Mitochondrial Oxidative Stress by Calcium/Copper/Elesclomol Tri-Overloaded Nanocages for Osteosarcoma Immunotherapy via Immunogenic Cell Death

Guangyao Jiang, Fangming Zhang, Ziyi Wu, Xianghong Zhang, Jingxia Xu, Zhuyuan Peng, Guofeng Li, Guanghui Zhu,* Xing Wang,* and Wensheng Xie*

Cite This: https://doi.org/10.1021/acsnano.5c08243

Read Online

ACCESS | Metrics & More | Article Recommendations | Supporting Information

**ABSTRACT:** Osteosarcoma (OS) immunotherapy offers a solution to overcome the limitations of traditional treatments. However, OS is a "cold tumor" due to deletion of the MTAP gene and sparse infiltration of immune cells, exhibiting high immunological tolerance. Here, we construct calcium/copper/elesclomol ($Ca^{2+}$/$Cu^{2+}$/STA-4783) tri-overloaded nanocages (SACCT NCs) to target mitochondrial oxidative stress and induce immunogenic cell death (ICD) for OS immunotherapy. In this pH-responsive nanoplatform, $Ca^{2+}$ and STA-4783 are codelivered to mitochondria, promoting $H_2O_2$ overexpression via the TCA cycle and SOD1. Subsequently, $Cu^+$ released from SACCT NCs effectively catalyzes $H_2O_2$ into toxic •OH, inducing oxidative stress damage and mitochondrial dysfunction rather than triggering cuproptosis (weak cuproptosis). Meanwhile, increased $Cu^+$ levels from transmembrane transport by CTR1 and ATP7A/B enhance intracellular oxidative stress, resulting in the ICD of OS cells. Finally, overexpression of CRT and NLRP3 activates the DCs−$CD8^+$ T cell immune response axis through the lymphocyte-mediated immunity pathway, enabling effective immunotherapy. Considering the *in vivo* pH-responsive biodegradability in the tumor immune microenvironment (TIME), our study has provided an impetus for the design and preparation of copper-based nanomaterials, which are efficacious in OS immunotherapy.

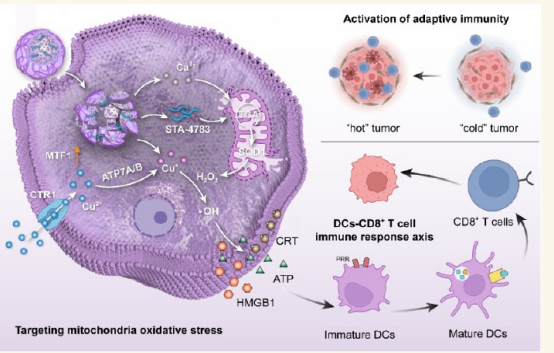


**KEYWORDS:** *Osteosarcoma, Immunotherapy, Oxidative Stress, Mitochondrial Oxidative Damage, Calcium/Copper/Elesclomol Triloaded*

## INTRODUCTION

Osteosarcoma (OS) is the most common primary malignant bone tumor, with a second peak of incidence in children, adolescents, and young adults and a median age of 16 years.[1,2] The clinical standard treatment for OS focuses on extensive surgical resection, adjuvant chemotherapy, and neoadjuvant chemotherapy.[3,4] Although the combination of polychemotherapy (high-dose methotrexate, doxorubicin, cisplatin, and ifosfamide) and surgery exhibits efficient therapeutic efficacy among patients with low-grade OS, the 5-year survival rate (less than 25%) has not improved significantly for patients with invasive, recurrent, or metastatic OS due to the development of resistance against antitumor medications.[5] Considering these barriers to traditional treatment regimens, it is of great significance to develop innovative and effective strategies to improve the therapeutic outcome and overall survival of patients with OS.

Nanomaterial-boosted immunotherapy for tumor treatment involves regulating the phenotype of immune cells, modulating the immunosuppressive tumor microenvironment,[6−8] and inhibiting immune checkpoints.[9−11] This not only results in the elimination of primary or distant metastatic tumors but also regulates the formation of immune memory to prevent tumor recurrence.[12] Therefore, immunotherapy for OS emerges as a

Received: May 18, 2025
Revised: October 17, 2025
Accepted: October 20, 2025

**Scheme 1. Schematic Illustration of Therapeutic Strategy by SACCT NCs for Osteosarcoma; a) Schematic Diagram of the Synthesis Process of SACCT NCs; b) Therapeutic Mechanisms of SACCT NCs through Targeting Mitochondrial Oxidative Stress and Immunotherapy by Tumor ICD**

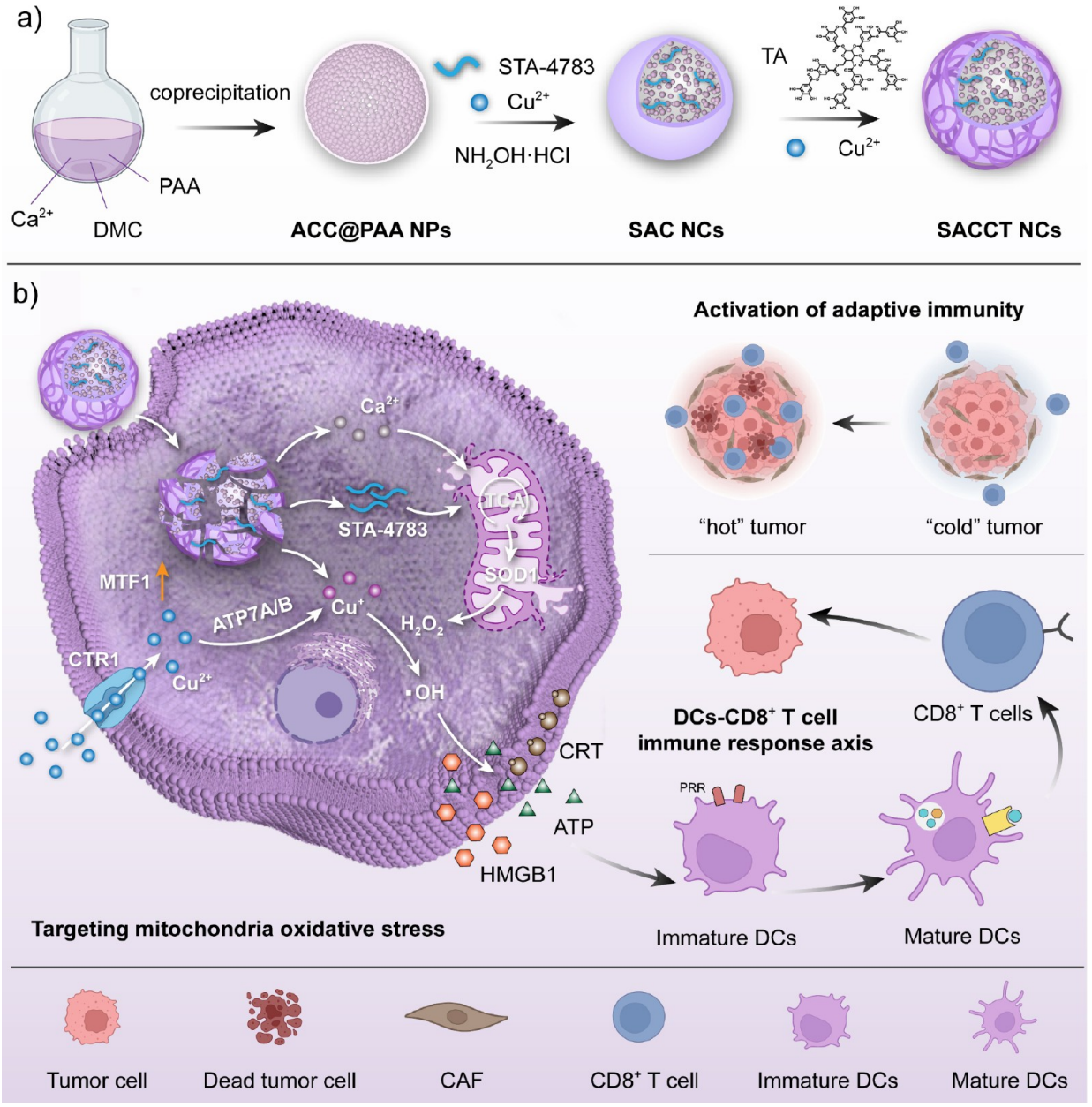


viable treatment modality capable of overcoming the drawbacks of conventional strategies while minimizing adverse effects and drug resistance, thus improving therapeutic effectiveness.[9,13] For example, the immune adjuvant mifamurtide is the most substantial therapeutic advance in OS in the past 10 years.[14] Furthermore, immune checkpoint inhibitors (ICIs), including programmed cell death protein-1 (PD-1), programmed cell death protein ligand-1 (PD-L1), and cytotoxic T lymphocyte-associated antigen-4 (CTLA-4) have been combined with other regimens to regulate the immune microenvironment of OS.[15] However, due to the deletion of the MTAP gene and few infiltration of immune cells, OS is regarded as a relatively "cold tumor" with strong immunological tolerance.[16,17] Therefore, altering the tumor immune microenvironment (TIME) by nanomaterials is widely recognized as a potential strategy to activate the body's defenses against OS.

Immunogenic cell death (ICD), which results from insufficient cellular adaptation to specific stressors, not only leads to cell death but also simultaneously regulates the release of damage-associated molecular patterns (DAMPs) from dying cancer cells to stimulate a systemic antigen-specific antitumor immune response and effectively overcome the immune tolerance of traditional treatments.[18−20] Therefore, nanomaterial-mediated tumor ICD will be a potential approach to overcome immunological tolerance and enhance therapeutic outcomes.[21] In this study, in order to target mitochondrial oxidative damage, we developed calcium/copper/elesclomol ($Ca^{2+}$/$Cu^{2+}$/STA-4783) tri-overloaded nanocages, designed as SACCT NCs, for ICD-mediated immunotherapy of OS with minimized systemic toxicity (Scheme 1). In this approach, ACC nanoparticles (ACC@PAA), which are GSH-responsive but stable under physiological conditions, were synthesized as a


https://doi.org/10.1021/acsnano.5c08243
ACS Nano XXXX, XXX, XXX−XXX

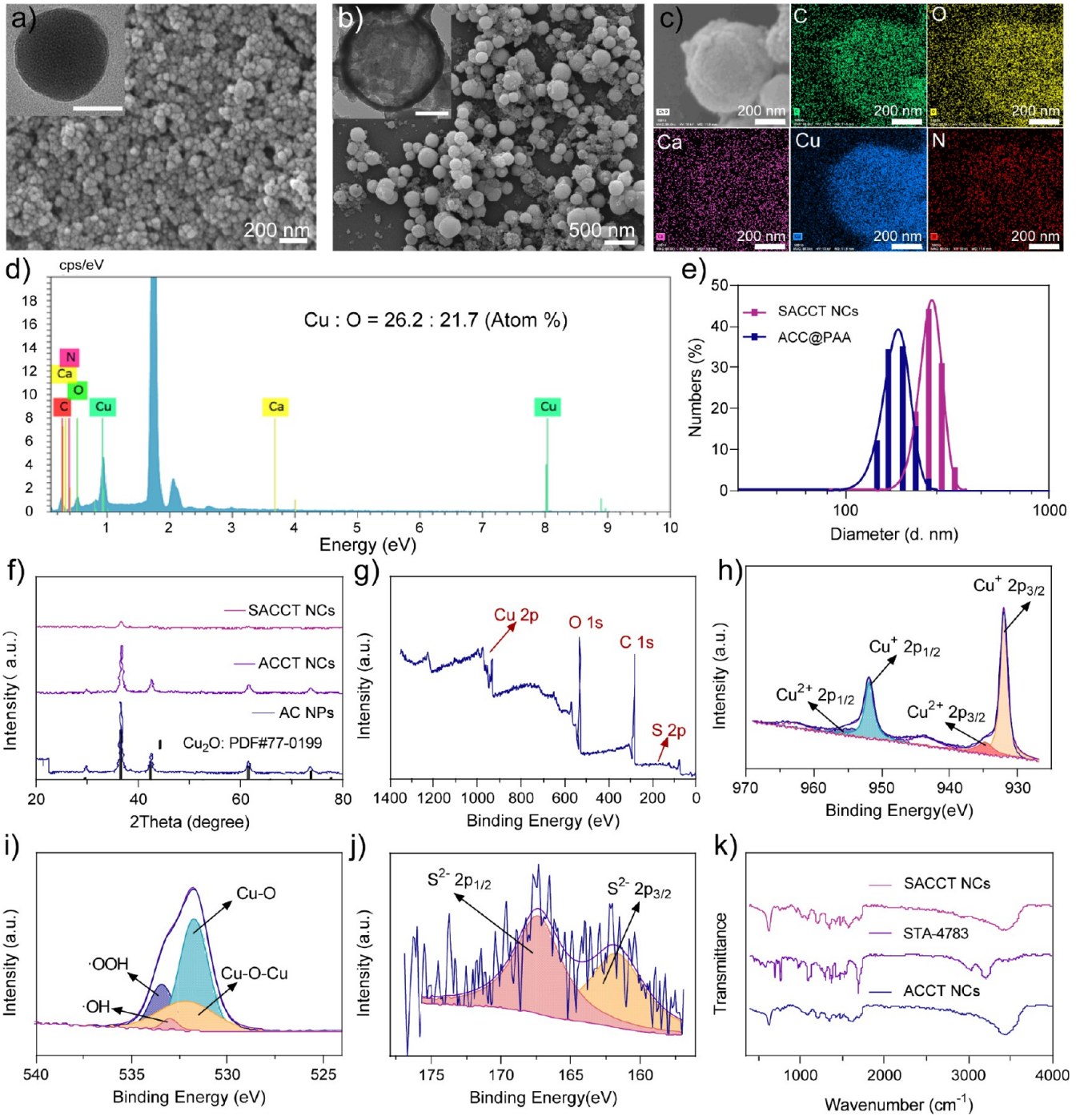


**Figure 1. Preparation and basic characterization of SACCT NCs. a) SEM and TEM (inset) images of ACC@PAA NPs; b) SEM and TEM (inset) images of SACCT NCs; c) element mapping (C, O, Ca, Cu, N); d) EDS spectrum of SACCT NCs; e) size distribution of both ACC@PAA and SACCT NCs in aqueous solution via DLS; f) XRD pattern of AC, ACCT, and SACCT NCs; g) XPS analysis of SACCT NCs; h–j) high-resolution Cu 2p (h), O 1s (i), and S 2p (j) XPS spectra of SACCT NCs; k) FTIR spectra of STA-4783, ACCT NCs, and SACCT NCs.**

template to synthesize STA-ACC@$Cu_2O$@Cu-TA nanocages (SACCT NCs) (Scheme 1a). Thus, $Ca^{2+}$ and STA-4783 were codelivered into mitochondria, inducing $H_2O_2$ overexpression through the tricarboxylic acid (TCA) cycle and superoxide dismutase 1 (SOD1) (Scheme 1b). Then, $Cu^+$ released from SACCT NCs effectively catalyzes $H_2O_2$ into toxic hydroxyl radicals (•OH) for inducing oxidative stress damage and mitochondrial dysfunction rather than cuproptosis (weak cuproptosis). Meanwhile, increased $Cu^+$ levels from transmembrane transport by copper transport protein 1 (CTR1) and ATP7A/B further enhance the intracellular oxidative stress, resulting in the ICD of OS cells. Finally, overexpression of calreticulin (CRT) and NLR family pyrin domain-containing 3 (NLRP3) activates the dendritic cells (DCs)–$CD8^+$ T cell immune response axis through the lymphocyte-mediated immunity pathway for efficient immunotherapy. Taken together, the design of pH-responsive biodegradable SACCT NCs provides an impetus to design copper-based nanomaterials for efficient OS immunotherapy.


https://doi.org/10.1021/acsnano.5c08243
ACS Nano XXXX, XXX, XXX−XXX

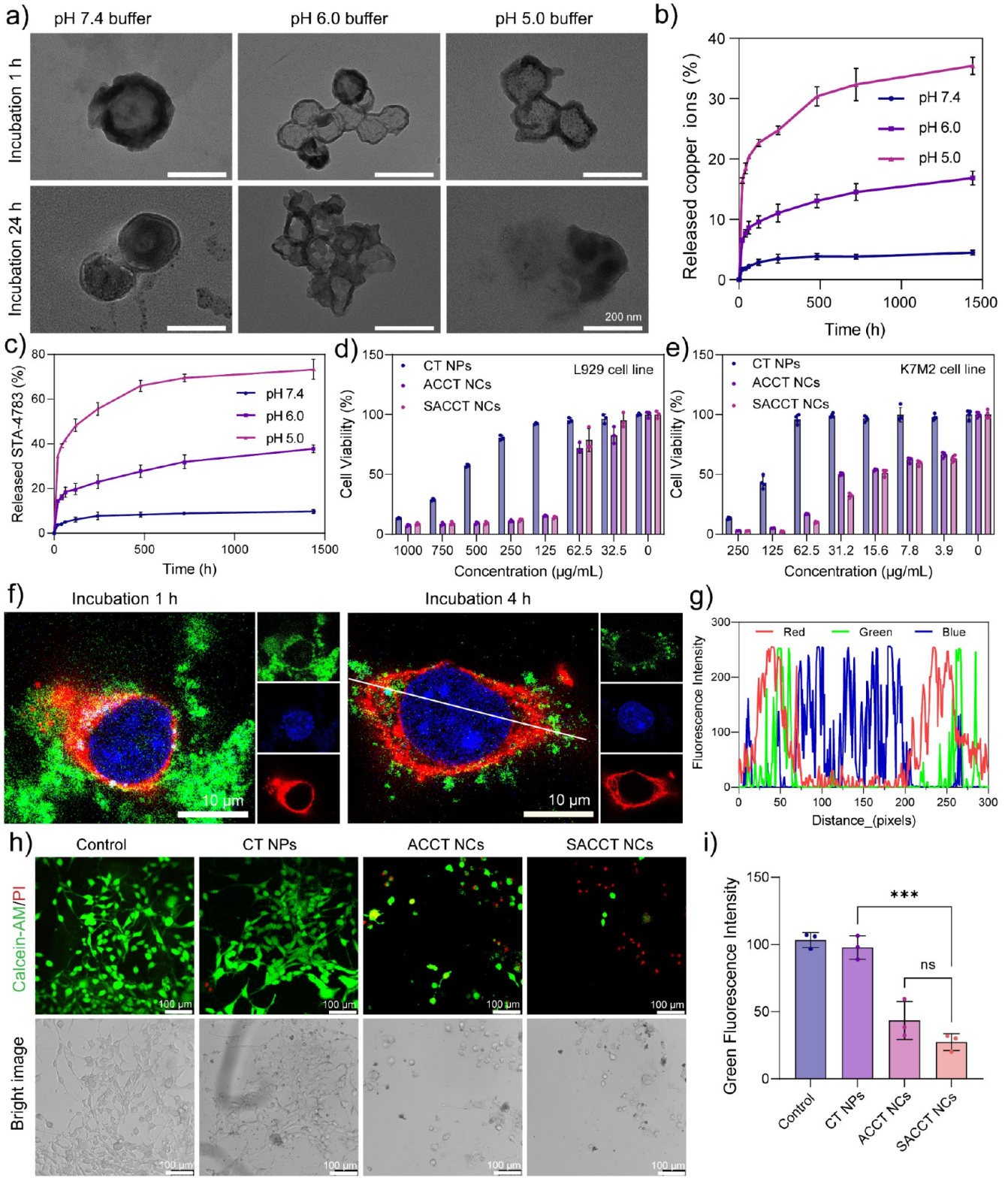


**Figure 2.** ***In vitro*** **biodegradability and cytotoxicity. a) TEM images of SACCT NCs in different pH buffers (7.4, 6.0, 5.0) incubated for 1 and 24 h; b,c) accumulative release of copper ions (b) and STA-4783 (c) from SACCT NCs in different pH buffers; d,e) cell viability (CCK-8) of L929 (d) and K7M2 (e) cells after incubation with various concentrations of culture medium CT, ACCT, and SACCT NCs for 24 h; f) confocal images of Coumarin-6-labeled SACCT NCs and K7M2 cells after coincubation for 1 and 4 h. The nucleus was stained with DAPI (blue), and the cytoskeleton was stained with rhodamine phalloidin (red); g) the signal intensity along the line in f; h,i) confocal images (h) and corresponding green fluorescence intensity (i) of K7M2 cells after treatment with PBS, CT NPs, ACCT NCs, and SACCT NCs for 24 h, and staining with calcein-AM (living cells) and PI (dead cells).**



https://doi.org/10.1021/acsnano.5c08243
*ACS Nano* XXXX, XXX, XXX−XXX

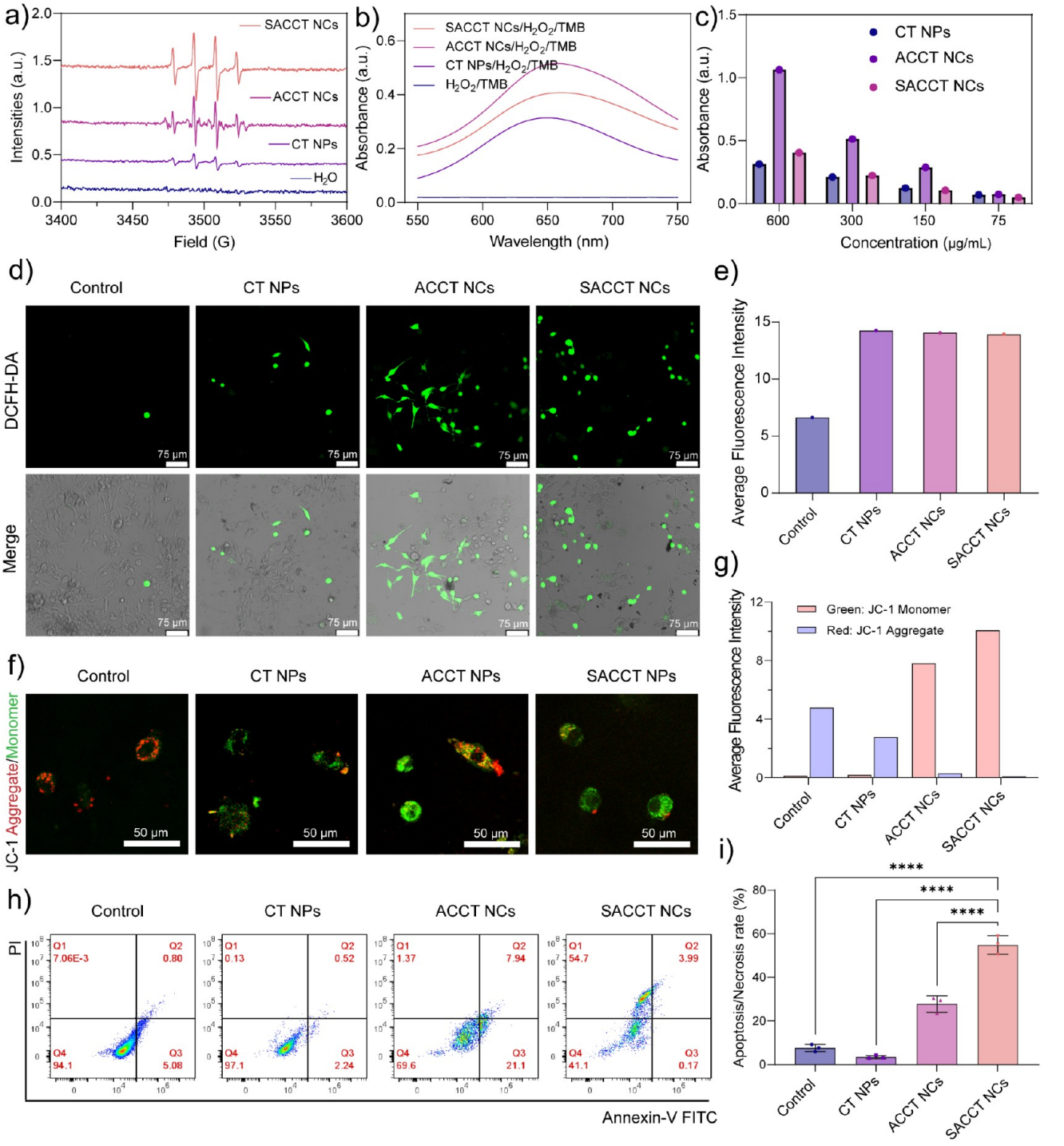


**Figure 3. POD-like catalytic activity and induced intracellular oxidative stress of SACCT NCs. a) ESR spectra of •OH radical generation by DMPO; b) vis−NIR absorbance of TMB in the presence of $H_2O_2$ and CT, ACCT, and SACCT NCs, respectively; c) vis−NIR absorbance of TMB at 652 nm in the presence of $H_2O_2$ and various concentrations (75, 175, 300, 600 $\mu$g/mL) of CT, ACCT, and SACCT NCs; d and e) confocal images (d) and corresponding fluorescence intensity (e) of K7M2 cells after treatment with PBS, CT, ACCT, and SACCT NCs, and then staining with DCFH-DA to exhibit the generation of intracellular ROS for 8 h; f and g) JC-1-stained confocal images (f) and corresponding fluorescence intensity (g) of K7M2 cells after treatment with PBS, CT, ACCT, and SACCT NCs for 8 h. h) Flow cytometry measurement of K7M2 cells after treatment with PBS, CT NPs, ACCT NCs, and SACCT NCs for 24 h, and then labeling with annexin V-FITC and PI. (i) The rate of apoptosis/necrosis cells.**

## RESULTS AND DISCUSSION

**Preparation and Characterization of SACCT NCs.** In order to codeliver $Ca^{2+}$ and $Cu^{+}$ ions within a single nanocarrier, amorphous calcium carbonate (ACC) and cuprous oxide nanoparticles were engineered and integrated via a template strategy. Specifically, poly(acrylic acid) (PAA)-coated ACC nanoparticles (ACC@PAA) were synthesized via a coprecipitation method. As shown in Figure 1a, homogeneously spherical nanoparticles were obtained with a narrow size distribution, and an obvious core (ACC)−shell (PAA) structure was presented in


https://doi.org/10.1021/acsnano.5c08243
ACS Nano XXXX, XXX, XXX−XXX

the TEM image. Then, STA-4783-loaded and copper-tannic acid (Cu-TA) phenolic network-modified STA-ACC@$Cu_2O$@Cu-TA nanocages (SACCT NCs) were synthesized via biomineralization by using ACC@PAA NPs as a template and further surface modification according to our previous studies.[22,23] The SEM and TEM images (Figure 2b) exhibited the hollow spherical structure of SACCT NCs with sparse inner ACC. Additionally, spherical CT NPs and hollow spherical $Cu_2O$ NCs were prepared as a reference (Figure S1, Supporting Information). Further element mapping and energy-dispersive X-ray spectroscopy (EDS)-based SEM clearly demonstrated the uniform distribution of carbon (C), oxygen (O), calcium (Ca), copper (Cu), and nitrogen (N), among which N is contributed by STA-4783, indicating successful encapsulation (Figure 1c and d). The semiquantitative analysis based on EDS showed that the atomic ratio of Cu/O was 26.2/21.7%), which is between 1/1 (CuO) and 2/1 ($Cu_2O$), confirming the components of cuprous ($Cu^+$) and cupric ($Cu^{2+}$) ions (Figure 1d). The results of dynamic light scattering (DLS) (Figure 1e) showed that the particle size increased from 176.61 nm (ACC@PAA) to 266.92 nm (SACCT), which was in agreement with the SEM images. The XRD diffraction (X-ray) patterns of as-prepared AC, ACCT, and SACCT NCs completely matched the standard $Cu_2O$ characteristic peaks (PDF#77−0199), confirming the major component of $Cu_2O$ shell (Figure 1f). In addition, the results of X-ray photoelectron spectroscopy (XPS) (Figure 1g−j), which declare the energy levels and binding energies of the elements, showed typical Cu 2p and S 2p from ACCT and STA-4783, respectively. The high-resolution Cu 2p (Figure 1h) demonstrated the high level of $Cu^+$ (932.15 and 951.95 eV) and low level of $Cu^{2+}$ (934.85 and 954.85 eV), indicating the $Cu_2O$ core and Cu-TA shell of the SACCT NCs. This was also verified by the Cu−O binding energy (531.77 eV) and the Cu−O−Cu binding energy (532.16 eV) in the high resolution O 1s (Figure 1i). The typical $S^{2-}$ binding energy (161.79 and 167.42 eV) (Figure 1j) indicated the successful loading of STA-4783 into the SACCT NCs. Since STA-4783 was loaded into the $Cu_2O$ hollow core, the Fourier transform infrared spectroscopy (FTIR) of SACCT NCs did not present the typical peaks compared with that of ACCT NCs.

**pH-Responsive Biodegradability and *In Vitro* Cytotoxicity.** As ACC and $Cu_2O$ could rapidly collapse under the influence of an external acidic environment, the pH-responsive biodegradability properties of SACCT NCs were evaluated in mimic blood (pH 7.4) and tumor tissue environments (pH 6.0 and 5.0).[22] As shown in Figure 2a, the nanocage structure of SACCT NCs was stable in pH 7.4 buffer for 24 h. However, the inner ACC and $Cu_2O$ core quickly degraded in pH 6.5 buffer for only 1 h, and the whole structure flattened after 24 h of incubation. When the pH buffer decreased to 5.0, the SACCT NCs totally collapsed, which will guarantee the *in vitro* biodegradability in the tumor microenvironment. Meanwhile, the accumulative release of copper ions from SACCT NCs was measured in different pH buffers (Figure 2b). The low level of release in pH 7.4 buffer confirmed the stable structure of as-synthesized nanocages in blood circulation. Approximately 16.86% and 35.45% of copper ions were released within 1,500 h of incubation in pH 6.0 and 5.0 environments, respectively. For STA-4783 to be physically loaded into the inner structure of the SACCT NCs, the accumulative release kinetics of STA-4783 under different pH buffers were similar to those of copper ions (Figure 2c). Based on these basic characteristics, the *in vitro* biocompatibility and cytotoxicity were assessed using mouse fibroblast (L929) and mouse osteosarcoma (K7M2) cell lines. As shown in Figure 2c, CT NPs exhibited relatively better biocompatibility with L929 cells compared to ACCT NCs and SACCT NCs. Luckily, all agents showed low in vitro cytotoxicity when the incubation concentration was reduced to 62.5 $\mu$g/mL. On the contrary, both ACCT NCs and SACCT NCs presented higher cytotoxicity in the K7M2 cell line, with low IC50 values of 15.79 and 11.35 $\mu$g/mL, respectively (Figure 2e), demonstrating the excellent antitumor efficacy of the as-synthesized SACCT NCs.

To evaluate the interaction between nanoagents and K7M2 cells, SACCT NCs were labeled with Coumarin-6 and cells were stained with DAPI (nucleus) and rhodamine phalloidin (cytoskeleton). As shown in Figure 2f, few SACCT NCs were taken up by cells after 1 h incubation, and the amount increased significantly 4 h later, indicating an effective endocytosis process. Furthermore, the well-matched colocalization curve (Figure 2g) further denotes the interaction process. Additionally, a calcein-AM/PI cell cytotoxicity assay kit was used to visually assess the in vitro cytotoxicity of SACCT NCs. Compared with the control group, CT NPs showed negligible cytotoxicity (Figure 2h and Figure S2 and Supporting Information) with strong green fluorescence. In contrast, both ACCT NCs and SACCT NCs treated K7M2 cells presented a lower survival rate (Figure 2h and i), demonstrating efficient *in vitro* antitumor efficacy. Furthermore, SACCT NCs exhibited a better effect than ACCT NCs due to the additional assistance of STA-4783.

**POD-Like Catalytic Activity and Induced Intracellular Oxidative Stress.** The efficient antitumor effect of SACCT NCs inspires us to further explore the intracellular killing mechanism. As we know, $Cu^+/Cu^{2+}$ exhibits excellent Fenton/Fenton-like catalytic performance in the field of biocatalysis.[24,25] Thus, electron spin resonance (ESR) spectroscopy was employed to measure the catalytic activity of SACCT NCs using 5,5-dimethyl-1-pyrroline *N*-oxide (DMPO) as a spin probe. A typical ESR signal with an integral intensity ratio of 1:2:2:1 was observed for CT NPs, ACCT NCs, and SACCT NCs (Figure 3a), indicating the POD-like activity (hydroxyl radical, •OH) of the as-synthesized agents. Furthermore, both SACCT NCs and ACCT NCs exhibited stronger signal intensity than CT NPs because of the additional $Cu_2O$ components.

Based on these, the POD-like catalytic activity was measured by 3,3′,5,5′-tetramethylbenzidine (TMB) colorimetric assays.[26] In the presence of $H_2O_2$, SACCT NCs, ACCT NCs, and CT NPs could catalyze TMB oxidation to blue oxidized TMB (oxTMB), which presented an ultraviolet−visible (UV−vis) absorption peak at 652 nm, indirectly indicating the generation of •OH (Figure 3b). Additionally, the oxTMB absorbance gradually elevated as the concentration of nanoagents increased from 75 to 600 $\mu$g/mL (Figure 3c), which was ascribed to the generation of more •OH. Considering the efficient endocytosis performance, intracellular reactive oxygen species (ROS) generation in K7M2 cells was tested by the universal fluorescent indicator 2,7-dichlorodihydrofluorescein diacetate (DCFH-DA). As shown in Figure 3d, the CLSM images presented that CT NPs-treated K7M2 cells showed increased green fluorescence compared to the control group. Moreover, the highest green fluorescence was detected in either ACCT NCs-treated cells or SACCT NCs-treated cells (Figure 3e), which contributed to the high POD-like activity of $Cu_2O$. ROS is an essential adaptive mitochondrial signal triggered by various stressors, and intracellular ROS boosting will cause mitochondrial damage.[27,28] To evaluate the dysfunction of mitochondria


https://doi.org/10.1021/acsnano.5c08243
ACS Nano XXXX, XXX, XXX−XXX

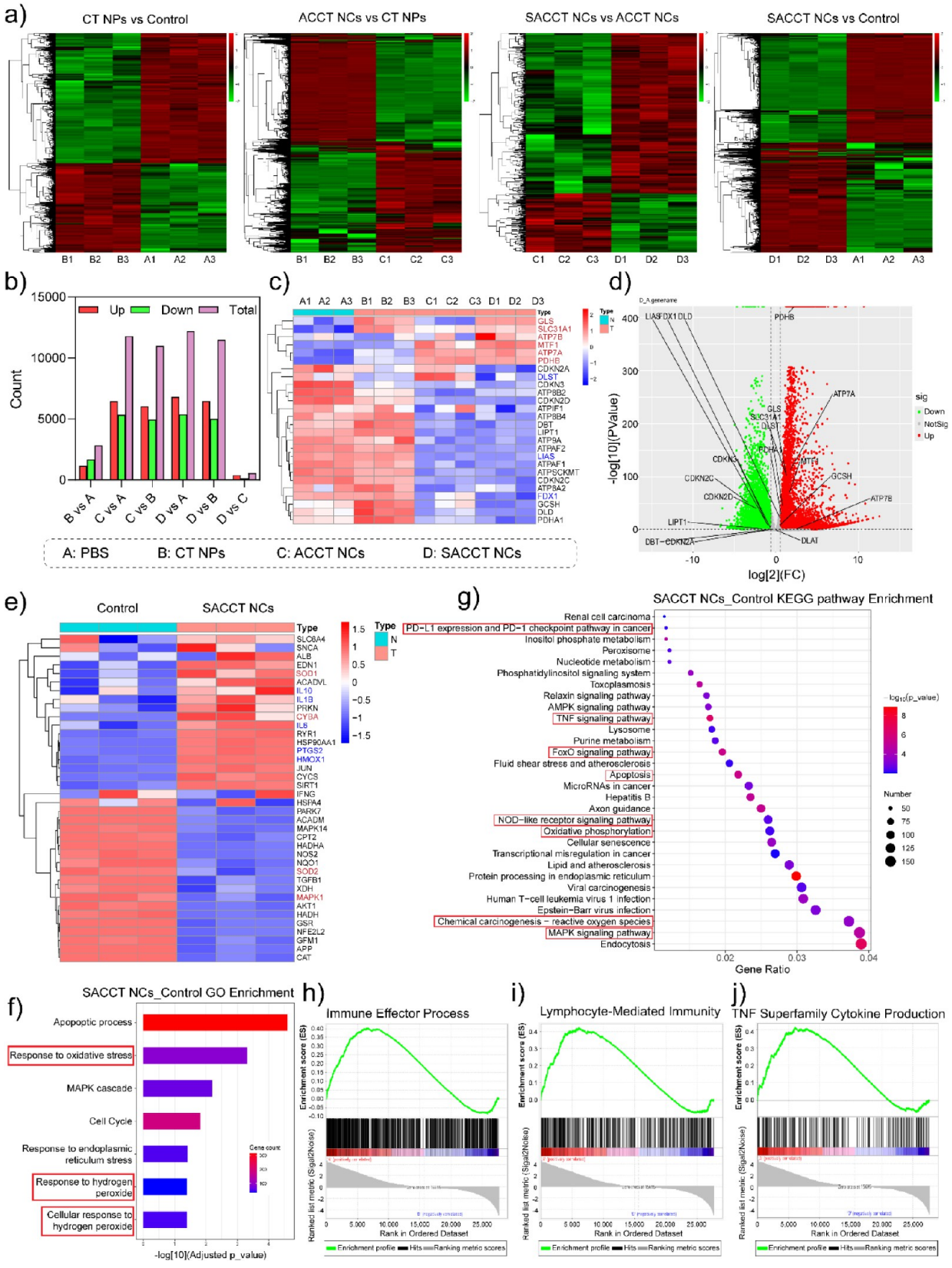


**Figure 4. Transcription analysis of K7M2 cells by RNA-seq upon various treatments. a) Heat map of gene expression for cells treated with PBS, CT NPs, ACCT NCs, and SACCT NCs; b) upregulated and downregulated gene expression after different treatments; c) heat map of gene expression for cells related to the cuproptosis pathway; d) volcano plots displaying the differentially expressed genes related to the cuproptosis pathway in SACCT NCs vs the control group; e) heat map of gene expression for cells in control and SACCT NCs groups related to intracellular oxidative stress; f, g) GO pathway (f) and KEGG pathway (g) enrichment analysis of DEGs in SACCT NCs vs the control group. h–j) GSEA showing the gene sets of immune effector processes (h), lymphocyte-mediated immunity (i), and TNF superfamily cytokine production (j) in SACCT NCs vs the control group.**



https://doi.org/10.1021/acsnano.5c08243
*ACS Nano* XXXX, XXX, XXX–XXX

after treatment with different agents, the fluorescent indicator JC-1 probe was applied to assess the mitochondrial membrane potential ($\Delta\Psi m$) change, which exhibited red fluorescence (high $\Delta\Psi m$) in healthy mitochondria and changed to green fluorescence (low $\Delta\Psi m$) in damaged mitochondria. Compared to the cells in the control group, both ACCT NCs and SACCT NCs-treated cells displayed strong green fluorescence and weakened red fluorescence (Figure 3f), indicating that the mitochondrial membrane potential was largely depolarized. Quantitative analysis declared that the ratio of green (JC-1 monomer) to red (JC-1 aggregate) in the SACCT NCs group was 3,000 times higher than that in the control group (Figure 3g and Figure S3), demonstrating severely damaged mitochondria. Furthermore, cellular apoptosis/necrosis was detected by the Annexin V-FITC/PI apoptosis detection kit. Flow cytometry results (Figure 3h) revealed an increase in early apoptotic cells in the ACCT NCs-treated group compared to the control and CT NPs groups. Meanwhile, about 54.7% necrotic cells were detected after treatment with SACCT NCs due to the assistance of loaded STA-4783 drugs. These findings demonstrated that SACCT NCs treatment exerts an antitumor effect by inducing oxidative stress damage and mitochondrial dysfunction.

**Transcription Analysis of SACCT NCs-Mediated Tumor Therapy.** To reveal the underlying antitumor mechanisms of SACCT NCs by inducing oxidative stress and mitochondrial dysfunction, high-throughput RNA-seq analysis was carried out to explore the changes of gene expression and signaling pathways (Figure S4, Supporting Information).[29] First, heat map analysis was employed to comprehensively analyze the differences in gene expression among the control, CT NPs, ACCT NCs, and SACCT NCs groups (Figure 4a). Compared with the control group, a total of 2,834, 11,804, and 12,179 differentially expressed genes (DEGs) were expressed for the CT NPs, ACCT NCs, and SACCT NCs groups, respectively (Figure 4b). The ACCT NCs group exhibited 6,040 upregulated DEGs and 4,944 downregulated DEGs compared with the CT NPs group, demonstrating that the $Cu_2O$ core played a key role in regulating tumor cells compared to the surface Cu-TA metal-phenolic network. In contrast, only 403 upregulated DEGs and 148 downregulated DEGs were detected in the SACCT NCs group when compared with the ACCT NCs group, indicating that STA-4783 slightly influenced gene expression during treatment. In recent years, chemotherapeutic drugs and Cu-based nanomaterials have been applied as nanomedicine to induce cuproptosis for efficient tumor treatment.[30−33] Therefore, in order to identify whether the as-synthesized SACCT NCs will trigger cuproptosis in OS, the expression of cuproptosis-related genes (FDX1, LIAS, DLAT, LIPT1, GLS, SLC31A1, ATP7A, ATP7B, ATP8A2, ATP8B2, ATP8B4, ATP9A, ATPAF1, ATPAF2, MTF1, PDHA1, PDHB, CDKN2A, CDKN2C, CDKN2D, CDKN3, ATPIF1, DBT, ATPSCKMT, GCSH, DLD) was checked in DEG set of CT NPs-, ACCT NCs-, and SACCT NCs-treated cells.[34,35] As shown in Figure 4c, upregulated ferredoxin 1 (FDX1) and lipoyl synthase (LIAS) gene expressions were clearly detected in CT NPs-treated cells, indicating that the Cu-TA metal-phenolic network could effectively induce OS cuproptosis via delivering $Cu^{2+}$ ions.[30,36] However, both ACCT NCs- and SACCT NCs-treated K7M2 cells presented downregulated expression of FDX1, LIAS, and dihydrolipoamide dehydrogenase (DLAT) genes (Figure 4c and d), demonstrating that both ACCT NCs- and SACCT NCs-induced cell death were not mainly contributed by the cuproptosis-mediated pathway. In contrast, glutaminase (GLS), solute carrier family 31 member 1 (SLC31A1), ATP7A, ATP7B, metal-response element-binding transcription factor 1 (MTF1), and pyruvate dehydrogenase E1-beta subunit (PDHB) genes were significantly upregulated after SACCT NCs treatment (Figure 4d). It is well known that SLC31A1, ATP7A, and ATP7B genes play key role in the transmembrane transport and intracellular homeostasis of copper ions.[37] The upregulated SLC31A1 gene promotes the transmembrane transport of $Cu^{2+}$ into cells by copper transport protein 1 (CTR1). Meanwhile, MTF1 can sense changes in the levels of metal ions (such as zinc, copper, and cadmium) within the cell and regulate the expression of related genes to maintain the homeostasis of intracellular metal ions.[38] GLS and PDHB participate in the tricarboxylic acid cycle (TCA cycle), generating a large amount of ATP to provide energy for cells, thus meeting the energy and biosynthesis requirements of rapidly proliferating tumor cells.[39,40] These changes were in agreement with the *in vitro* performance of oxidative stress damage and mitochondrial dysfunction caused by excessive or deficient metal ions.

In our previous study, the dual-overloaded $Ca^{2+}/Cu^{+}$ will effectively simulate extra $H_2O_2$ generation from mitochondria and then boost intracellular ROS levels to kill tumor cells via a Fenton-like reaction.[22] Meanwhile, STA-4783 can specifically bind to cardiolipin to target and localize to the mitochondrial membrane, thereby regulating the functions of membrane proteins and stabilizing the mitochondrial membrane structure.[41] Meanwhile, STA-4783 can also promote the appropriate uptake of calcium ions by mitochondria and induce efficient mitochondrial calcium overload. Further heat map analysis (Figure 4e) exhibited that SOD1 and Cytochrome *b*-245 alpha polypeptide (CYBA) genes were significantly upregulated in SACCT NCs groups compared to the control group, indicating the excessive generation of intracellular ROS caused by calcium/copper dual-overloading and STA-4783 release. Subsequently, Gene Ontology (GO) enrichment analysis was used to investigate the potential biological functions. As shown in Figure 4f, the DEGs in the SACCT NCs group were greatly involved in the apoptotic process, response to oxidative stress, response to hydrogen peroxide, and cellular response to hydrogen peroxide, directly confirming the oxidative stress damage-related genes (SOD1 and CYBA) upregulated expression. Besides, SACCT NCs-treated cells displayed obvious upregulated DEGs (IL10, IL1B, IL6, PTGS2, and HMOX1), which all are related to the inflammatory and immune response (Figure 4e). Further Kyoto Encyclopedia of Genes and Genomes (KEGG) pathway enrichment analysis revealed that genes related to the NOD-like receptor signaling pathway, FoxO signaling pathway, TNF signaling pathway, and PD-L1 expression and PD-1 checkpoint pathway in cancer were greatly affected by SACCT NCs (Figure 4g). Thus, we speculate that SACCT NCs treatment not only kills OS cells via inducing oxidative stress damage and mitochondrial dysfunction but also triggers an immune response. Gene set enrichment analysis (GSEA) of DEGs showed the upregulation of the immune effector process pathway, lymphocyte-mediated immunity pathway, and TNF superfamily cytokine production pathway, confirming the systemic immune response via SACCT NCs treatment.

***In Vivo* Biodistribution and Antitumor Efficacy Evaluation.** Motivated by the advanced *in vitro* therapeutic efficacy of SACCT NCs, a K7M2 tumor-bearing Balb/c mouse model was established to evaluate the *in vivo* antitumor efficacy


https://doi.org/10.1021/acsnano.5c08243
ACS Nano XXXX, XXX, XXX−XXX

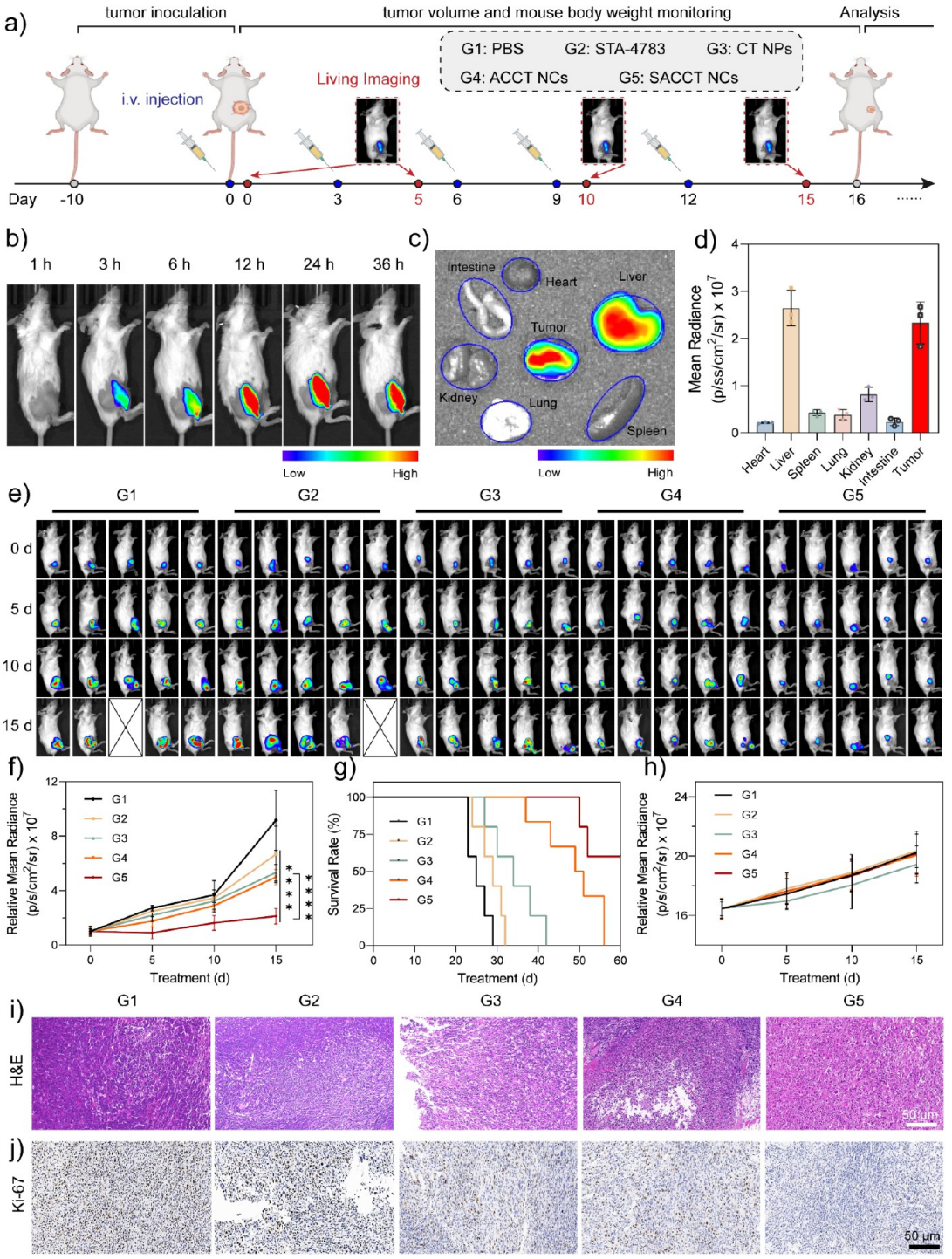


**Figure 5.** ***In vivo*** **biodistribution and antitumor efficacy of SACCT NCs. a) Schematic illustration of the** ***in vivo*** **antitumor therapy on the K7M2 tumor-bearing Balb/c mouse model; b) fluorescence bioimages of K7M2 tumor-bearing mice at various time points (1, 3, 6, 12, 24, 36 h) after intravenous injection with Cy5.5-labeled SACCT NCs; c) fluorescence bioimages of major organs after intravenous injection with Cy5.5-labeled SACCT NCs for 36 h; d) the average fluorescence intensity of Cy5.5-labeled SACCT NCs in tumor tissue and major organs at 36 h postinjection; e) luminescence images (Lumina IVIS system) of Balb/c mice bearing orthotopic K7M2-Luc osteosarcoma tumors during various treatments on days 0, 5, 10, and 15 using the Lumina IVIS system; f) quantified luminescence levels of tumor sites to exhibit the tumor size; g) Kaplan−Meier analysis of mouse survival rates after various treatments; h) body weight changes of mice during 15 days' treatment; i and j) H&E staining (i) and IHC staining ($K_i$-67) (j) of tumor tissues in various groups after 15 days' treatment.**

(Figure 5a). Before the therapeutic treatment, SACCT NCs were labeled with Cy5.5 dye and injected into tumor-bearing mice by intravenous (*i.v.*) injection via the caudal vein to measure the *in vivo* biodistribution at different time points. The fluorescent images showed that SACCT NCs highly targeted tumor tissues 3 h after iv injection (Figure 5b). The fluorescent intensity of tumor tissues gradually increased and reached its peak around 24 h (Figure S5 and Supporting Information). 36 h later, strong fluorescence from Cy5.5-labeled SACCT NCs still existed in tumor tissues (Figure 5c, and d), demonstrating that


https://doi.org/10.1021/acsnano.5c08243
ACS Nano XXXX, XXX, XXX−XXX

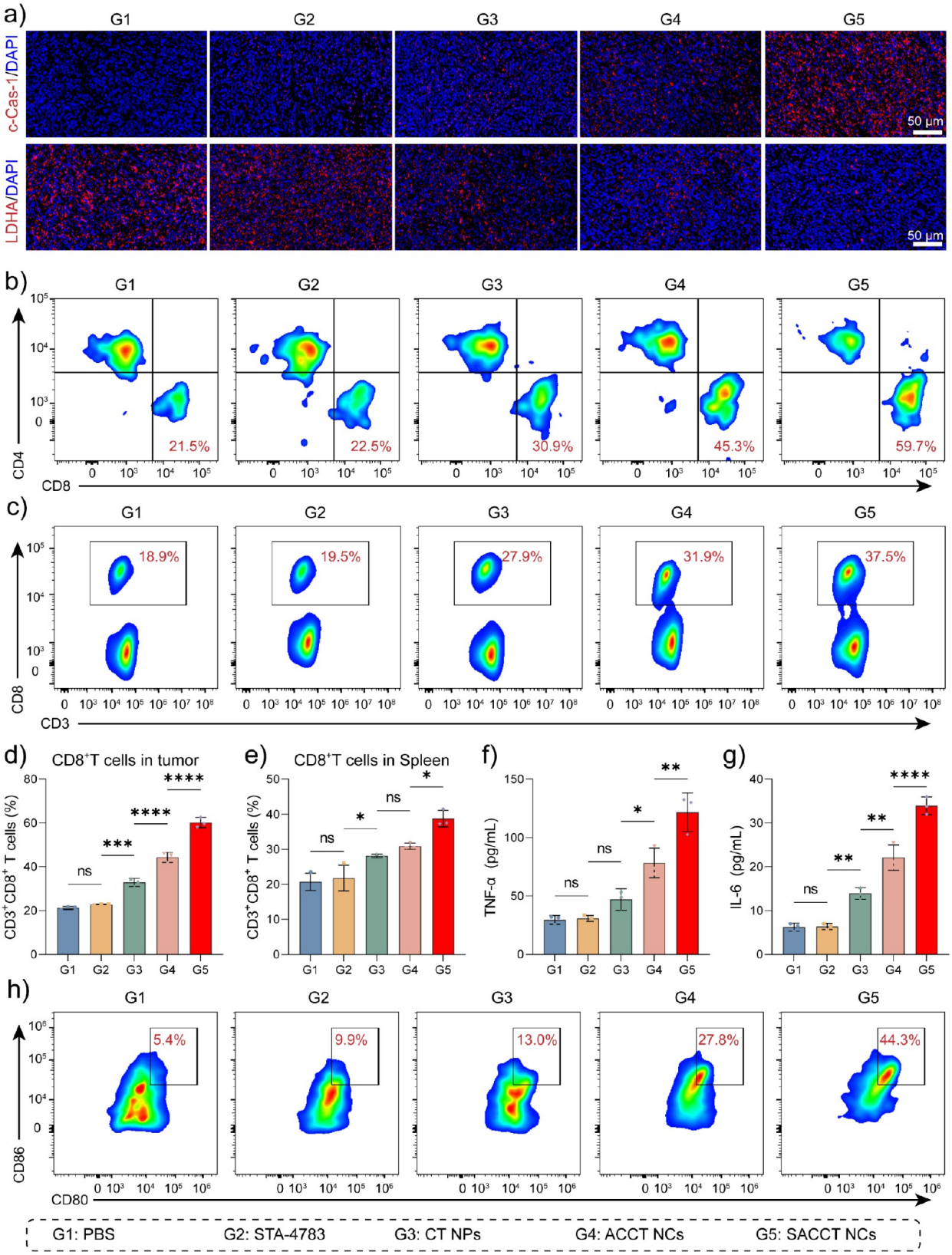


**Figure 6.** ***In vivo*** **antitumor immune response activation triggered by SACCT NCs' treatment. a) c-Cas-1 and LDHA expression within tumor tissues after various treatments via fluorescence staining. The nucleus was stained with DAPI (blue) to locate the tumor cells; b) the representative FCM analysis images of $CD4^+$ and $CD8^+$ T cells gating on $CD45^+CD11b^-CD3^+$ cells within tumor tissues after various treatments; c) the representative FCM analysis images of $CD8^+$ T cells gating on $CD45^+CD3^+$ cells in the spleen after various treatments; d,e) quantitative analysis of $CD8^+$ T cells within tumor tissues (d) and spleen (e) after various treatments via flow cytometry; f, g) the amount of cytokine IL-6 (f) and TNF-α (g) in serum after various treatments; h) the representative FCM analysis images of mature DC ($CD80^+CD86^+$) gating on $CD45^+CD11b^+CD11c^+$ cells within tumor tissues after various treatments.**



https://doi.org/10.1021/acsnano.5c08243
*ACS Nano* XXXX, XXX, XXX−XXX

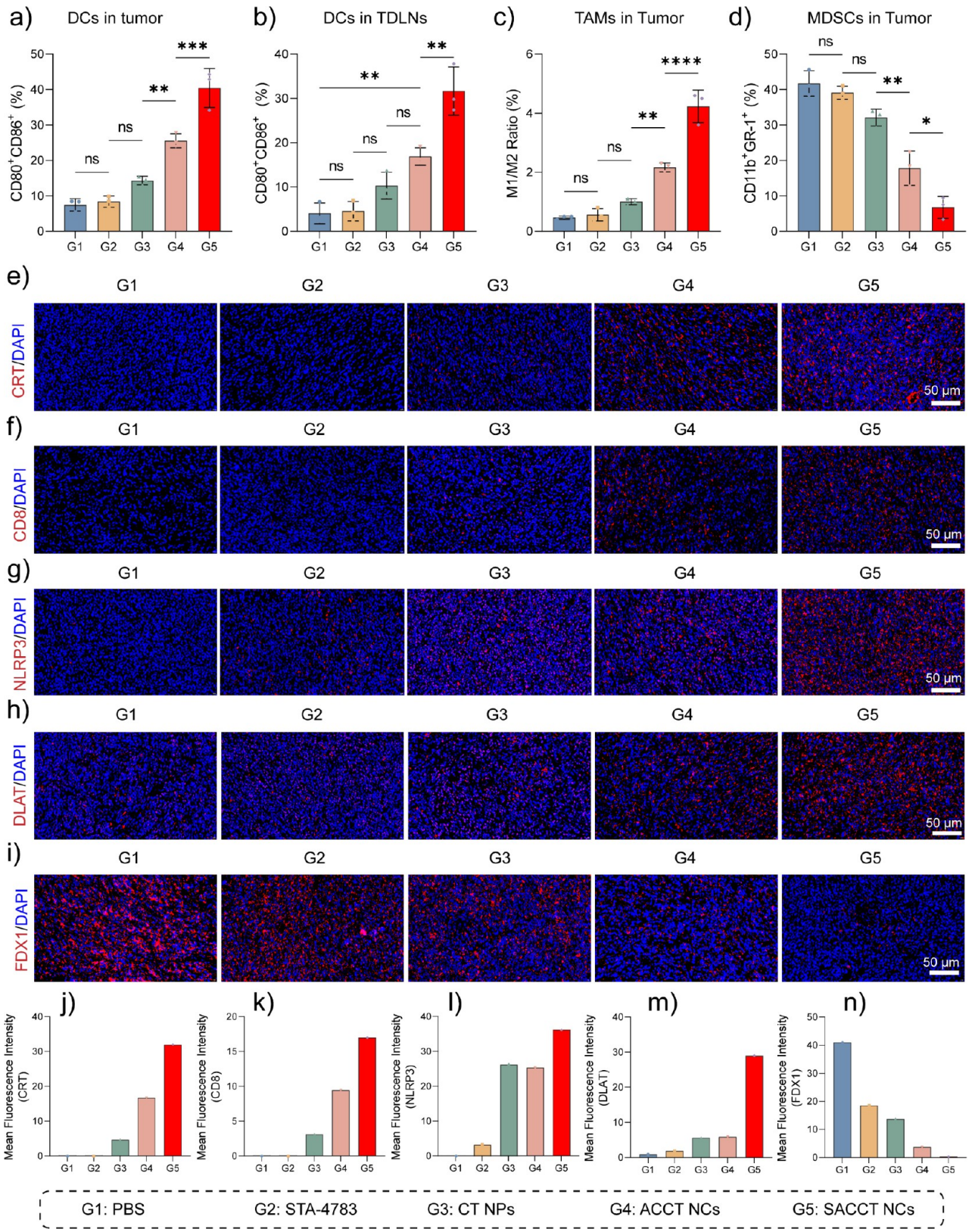


**Figure 7. Immune response and immunofluorescence analysis of the tumor tissues after SACCT NCs' treatment. a, b) Quantitative analysis of mature DCs within tumor tissues (a) and TDLNs (b) after various treatments via flow cytometry; c) quantitative analysis of the M1/M2 ratio for macrophages within tumor tissues after various treatments via flow cytometry; d) the percentage of MDSCs within tumor tissues after different treatments; (e−n) fluorescence staining images and corresponding quantitative analysis of CRT (e,j), CD8 (f,k), NLRP3 (g,l), DLAT (h,m), and FDX1 (I,n) expression within tumor tissues after various treatments. The nucleus was stained with DAPI (blue) to locate the tumor cells.**



https://doi.org/10.1021/acsnano.5c08243
*ACS Nano* XXXX, XXX, XXX−XXX

the as-synthesized SACCT NCs could effectively target tumors under the action of the passive targeting process,[42,43] which provides a solid guarantee for *in vivo* therapeutic efficacy via *i.v.* administration. When the tumor volume reached about 100 $mm^3$, the mice were randomly divided into five groups ($n = 5$) as follows: G1) PBS, G2) STA-4783, G3) CT NPs, G4) ACCT NCs, and G5) SACCT NCs. During the therapeutic procedure, mice were i.v. injected with 100 $\mu$L of PBS, STA-4783, CT NPs, ACCT NCs, and SACCT NCs (10 mg/kg) on days 0, 3, 6, 9, and 12. For K7M2-Luc OS, tumor cells were integrated with luciferin (Luc), the changes of tumor growth were recorded through the Lumina IVIS system (Figure 5e). As a result, compared to the rapid growth rate in the PBS group, mice in STA-4783, CT NPs, and ACCT NCs groups presented effective growth inhibition of tumor tissues during 15 days' treatment (Figure 5f).

It is worth noting that the SACCT NCs group presented a high suppression rate of about 76.8% compared with the PBS group. Moreover, mice in the SACCT NCs group demonstrated a 31.2% higher inhibition rate of tumor growth than that in ACCT NCs (45.6%), revealing that STA-4783 effectively synergizes with the oxidative stress damage process caused by calcium/copper dual-overload. In addition, the survival rate of the SACCT NCs group was as high as 60% during 60 days' observation period (Figure 5g), which means that the induced immune response continuously made a difference. Compared with the PBS group, the average body weight of mice in various treatment groups did not show any significant difference (Figure 5h), demonstrating the limited adverse effects and excellent *in vivo* biosafety of the treatment. Further hematoxylin and eosin (H&E) staining images of tumor tissues in various treatment groups presented the most severe tumor necrosis in the SACCT NCs group (Figure 5i), confirming its powerful therapeutic efficacy. Meanwhile, the H&E images of main organs (heart, liver, spleen, lung, and kidney) (Figure S6, Supporting Information) further verified the *in vivo* biocompatibility of the as-synthesized SACCT NCs. Immunohistochemistry analysis ($K_i$-67) (Figure 5j) of tumor tissues presented a high proliferation rate of cells in the PBS group and significantly inhibited cell proliferation in the SACCT NCs group, revealing the efficient antitumor effect.

In addition, biochemical analysis of whole blood and serum of various agent-treated mice was employed to evaluate biosafety. Compared with the PBS group, only the number of white blood cells (WBC) slightly increased in the STA-4783, ACCT NCs, and SACCT NCs groups due to the stress response to administration (Figure S7). There was no significant difference in the levels of red blood cells (RBC), lymphocytes, monocytes (Mon), hemoglobin (HGB), mean corpuscular volume (MCV), mean corpuscular hemoglobin (MCH), mean corpuscular hemoglobin concentration (MCHC), and blood platelets (PLT). Meanwhile, the biochemical measurement of serum (Figure S8) in various groups presented normal levels of blood urea nitrogen (BUN), serum creatinine (CR), alkaline phosphatase (ALP), total bilirubin (TBIL), aspartate aminotransferase (AST), and alanine aminotransferase (ALT), demonstrating the excellent biosafety of the as-synthesized nanoagents. All of the above results demonstrate that SACCT NCs possess great potential to efficiently cure OS with low systemic toxicity.

***In Vivo* Antitumor Immunity Measurement.** Cleaved caspase-1 (c-cas-1) is a key effector molecule after the activation of the inflammasome.[44] Through the regulation of the inflammatory response, immune cells are recruited to the tumor tissue to mediate the immune response. Compared with the tumor tissue in the PBS group, the ACCT NCs-treated group exhibited obvious overexpression of c-cas-1 (Figure 6a). Moreover, tumor tissues in the SACCT NCs-treated group presented the highest level of c-cas-1 expression, confirming the immune response triggered by SACCT NC treatment. Meanwhile, lactate dehydrogenase A (LDHA) is highly expressed during tumor cell glycolysis (Warburg effect).[45] It provides energy and metabolic intermediates for the rapid proliferation of tumor cells, promoting tumor growth, invasion, and metastasis. It is clear that agent-treated groups displayed a decreased level of LDHA (Figure 6a), verifying the effective antitumor effect. Transcription analysis has demonstrated that SACCT NCs treatment could effectively induce lymphocyte-mediated immunity. Thus, the dendritic cell (DC)−$CD8^+$ T cell immune response axis was systematically explored via flow cytometry. As shown in Figure 6b and Figure S9, SACCT NC administration significantly expanded $CD8^+$ ($CD45^+CD11b^-CD3^+CD8^+$ gate) cytotoxic T cell subsets (59.7%) in tumors compared with PBS treatment (21.5%). The $CD8^+/CD4^+$ T cell ratio, a critical prognostic indicator for immunotherapy outcomes, significantly increased with SACCT NCs treatment (Figure 6d). In particular, the $CD8^+$ ($CD45^+CD3^+CD8^+$ gate) cytotoxic T cell subsets in the spleen of the SACCT NCs group were about 37.5%, which was about 2-fold higher than that in the PBS group (Figure 6c and e and Figure S10). Meanwhile, ELISA results presented significant overexpression of TNF-$\alpha$ and IL-6 cytokines (Figure 6f and g). Besides, an obvious increase in the expression of IFN-$\gamma$ and IL-1$\beta$ was detected in the SACCT NCs group compared to the control group (Figure S11), indicating the activation of T cells, DCs, and macrophages for the antitumor effect via systemic immunotherapy. Furthermore, in the TIME, elevated expression of costimulatory molecules CD80/CD86 ($CD45^+CD11b^+CD11c^+CD80^+CD86^+$ gate) on DCs in the SACCT NCs-treated group was detected (Figure 6h and Figure S12). This finding aligns well with the significant increase in the number of tumor-infiltrating $CD8^+$ T cells observed in mice treated with SACCT NCs. In contrast, treatment with STA-4783 or CT NPs alone did not present effective DC maturation compared with the PBS group (Figure 7a), confirming that ICD was contributed by the combination of $Ca^{2+}/Cu^+$ dual ions and STA-4783.

**Induced Immunogenic Cell Death by SACCT NCs Treatment.** To conduct a more in-depth evaluation of the capacity of SACCT NCs to activate antigen-presenting cells in the *in vivo* setting, tumor-draining lymph nodes (TDLN) were isolated from mice and subjected to flow cytometric analysis (Figure 7b and Figure S13, Supporting Information). The percentage of mature DCs ($CD45^+CD11b^+CD80^+CD86^+$ gate) in the TDLN of SACCT NCs-treated mice was 6.8-fold higher compared with that of PBS-treated mice and 1.9-fold higher than that of mice treated with ACCT NCs. Intravenous administration of SACCT NCs facilitated the M2-to-M1 ($CD45^+CD11b^+F4/80^+CD80^+$ gate for M1, $CD45^+CD11b^+F4/80^+CD206^+$ gate for M2) repolarization of macrophages within the tumor, as depicted in Figure 7c and Figure S14−S16. Furthermore, obviously increased IL-12 (secreted by M1 macrophages) and decreased IL-10 (secreted by M2 macrophages) and TGF-$\beta$ (secreted by M2 macrophages) levels were observed in the SACCT NCs-treated group compared to the control group (Figure S17, Supporting Information), confirming the M2-to-M1 repolarization of


https://doi.org/10.1021/acsnano.5c08243
ACS Nano XXXX, XXX, XXX−XXX

macrophages. Additionally, myeloid-derived suppressor cells (MDSCs) are recognized for their immunosuppressive functions and play a crucial role in tumor immune evasion. In this study, compared with other treatment modalities, SACCT NCs treatment led to a significant reduction in the infiltration of intratumoral MDSCs ($CD45^+CD11b^+Gr\text{-}1^+$ gate) (Figure 7d and Figure S18). Taken together, these findings offer strong and conclusive evidence that SACCT NCs initiate a potent immune activation cascade via ICD, which ultimately contributes to the continuous regression of tumors in the preclinical K7M2 model employed in this study.

CRT serves as an "eat-me" signal, which is recognized by the receptors on the surface of DCs.[46] This recognition promotes the phagocytosis of tumor cells by antigen-presenting cells and subsequently activates the body's antitumor immune response. Obvious overexpression of CRT was detected in both ACCT NCs- and SACCT NCs-treated groups (Figure 7e, j), verifying the ICD induced by agents' administration. These results were in agreement with the increased levels of mature DCs in both tumor tissues and TDLN (Figure 7a and b). The strong CD8 fluorescence intensity in the SACCT NCs group further confirmed the DCs-$CD8^+$ T cell immune response procedures (Figure 7f and k). Additionally, NOD-like receptor protein 3 (NLRP3) is an essential component of the inflammasome.[47] In the tumor microenvironment, various factors can activate the NLRP3 inflammasome, promoting the maturation and release of inflammatory cytokines and, in turn, recruiting immune cells to the tumor site and initiating an immune response. The immunofluorescence of NLRP3 staining images exhibited a strong signal in the SACCT NCs group compared with others (Figure 7g and l), confirming the immune response. *In vitro* transcription analysis has demonstrated that SACCT NCs-mediated ICD of OS was hardly related to cuproptosis. The immunofluorescence of DLAT (Figure 7h and m) and FDX1 (Figure 7i and n) in the SACCT NCs group demonstrated the most significant DLAT aggregation and dramatic FDX1 loss, revealing the coactivation of the cuproptosis pathway. Taken together, SACCT NCs-induced immunotherapy via ICD was mainly contributed by targeting mitochondrial oxidative stress and also by weak cuproptosis, providing a promising strategy for OS treatment.

## CONCLUSION

In conclusion, calcium/copper/STA-4783 tri-overloaded nanocages (SACCT NCs) were constructed to target mitochondrial oxidative stress, thereby inducing ICD for OS immunotherapy. In this pH-responsive nanoplatform, $Ca^{2+}$ and STA-4783 were codelivered into mitochondria, triggering the overexpression of $H_2O_2$ via the TCA cycle and SOD1. Subsequently, $Cu^+$ released from SACCT NCs effectively catalyzes $H_2O_2$ into toxic •OH for inducing oxidative stress damage and mitochondrial dysfunction without substantial cuproptosis (weak cuproptosis). Meanwhile, increased $Cu^+$ levels from transmembrane transport by CTR1, ATP7A, and ATP7B further exacerbated intracellular oxidative stress, culminating in the ICD of OS cells. Finally, overexpression of CRT and NLRP3 activates the DCs−$CD8^+$ T cell immune response axis through the lymphocyte-mediated immunity pathway, facilitating efficient immunotherapy. Overall, this *in vivo* pH-responsive biodegradable copper nanomaterial based on $Cu_2O$ demonstrated a unique potential to overcome the low response rate of OS immunotherapy via activation of the DCs−$CD8^+$ T cell immune response axis.

## METHODS AND EXPERIMENTAL SECTION

**Materials.** $CaCl_2$, $CuCl_2{\cdot}2H_2O$, $CH_3COONa{\cdot}3H_2O$, NaOH, dimethyl carbonate (DMC), poly(acrylic acid) (PAA), hydroxyamine hydrochloride, hydrogen peroxide, and ethanol were purchased from Sinopharm Chemical Reagent Co., Ltd. Elesclomol (STA-4783) and tannic acid (TA) were purchased from Shanghai Yuanye Biotechnology Co., Ltd. DMEM medium, penicillin-streptomycin, and fetal bovine serum (FBS) were brought from Wuhan Pricella Biotechnology Co., Ltd. CD45-APC-cy7, CD11b-FITC, Gr-1-BV650, CD80-BV421, CD86-PE, CD11c-PE-Dazzle594, F4/80-PE-cy7, CD206-AlexaFlour 647, CD3-PE-cy5, CD8-AlexaFlour 700, and CD4-Percp-cy5.5 mouse mAb were purchased from BioLegend. TMB single-component solution, Coumarin-6, Calcein-AM/PI double stain kit, reactive oxygen species assay kit (DCFH-DA), mitochondria membrane potential assay kit with JC-1, Annexin V-FITC/PI apoptosis detection kit, BCA protein assay kit, TNF-$\alpha$ ELISA kit, IL-6 ELISA kit, and Cell Counting Kit-8 (CCK-8) were brought from Beijing Suolaibao Technology Co., Ltd.

**Synthesis of ACC@PAA NPs.** A coprecipitation method was employed to synthesize ACC@PAA NPs. 184 mg of $CaCl_2$ was dissolved in 96 mL of absolute ethanol in a 250 mL round-bottom flask. Then, 32 mL of 0.1 M NaOH solution was added quickly under vigorous magnetic stirring. 32 mL of 0.02 mM DMC was added at a speed of 16 mL/h via a peristaltic pump. The reaction was kept for another 2 h before 530 $\mu$L of PAA solution was added. 6 h later, ACC@PAA NPs were obtained via centrifugation (5,000 rpm, 10 min) and washed with ethanol three times.

**Synthesis of SAT-ACC@$Cu_2O$ (SAC) Nanocages.** SAC NCs were synthesized via biomineralization by using ACC@PAA NPs as a template.[1] Specifically, 50 mg of ACC@PAA NPs were suspended in 86.2 mL of DI water in a 120 mL beaker. Then, 5 mg of STA-4783 was added and sonicated for complete dissolution. 5 min later, 5 mL of 0.1 M $CuCl_2$ solution was added and the system was left to stand for another 5 min. 1.8 mL of 1 M NaOH aqueous solution was slowly added to 12 mL of 0.1 M hydroxylamine hydrochloride solution. The system was kept for 12 h biomineralization at 37 °C. Finally, SAC NCs were obtained via centrifugation (10,000 rpm, 10 min) washed with DI water three times. The product was stored in PBS at 4 °C for further use.

**Synthesis of SAT-ACC@$Cu_2O$@Cu-TA (SACCT) NCs.** A 5 mL portion of 10 mg/mL SAC NPs solution was mixed with 1.2 mL of 1 mM TA solution under vigorous magnetic stirring. 20 min later, the final SACCT NCs were obtained via centrifugation (10,000 rpm, 10 min) and washed with DI water three times. The product was stored in PBS at 4 °C for further use.

**Synthesis of Cu-TA (CT) NPs.** 10.72 mg of $CuCl_2$ and 17 mg of TA were dissolved in 4 mL of DI water under vigorous magnetic stirring. Then, $NaHCO_3$ aqueous solution was added to adjust the pH = 8. 1 h later, CT NPs were obtained via centrifugation (10,000 rpm, 10 min) and washed with DI water three times. The product was stored in PBS at 4 °C for further use.

**Characterization.** The morphologies and structures of the as-synthesized SACCT NCs were measured by a scanning electron microscope (SEM, Hitachi) and a transmission electron microscope (TEM, Zeiss). The components of SACCT NCs were measured by an energy dispersive


https://doi.org/10.1021/acsnano.5c08243
ACS Nano XXXX, XXX, XXX−XXX

spectrometer (EDS, Hitachi). The size distribution was analyzed using dynamic light scattering (DLS, Malvern). The crystal structure was analyzed by powder X-ray diffraction (XRD, Bruker). The concentrations of metal ions in nanoparticles were measured by iCAP Q inductively coupled plasma mass spectrometry (ICP-MS). The chemical valence of Cu, O, and S was detected by Fourier transform infrared spectroscopy (FTIR, Bruker). All fluorescence images were acquired by a laser scanning confocal microscope (LSCM, Zeiss). Flow cytometry measurements were performed on a BD FACSAria Fusion instrument (BD Biosciences). Immunohistochemical images were obtained by a high-throughput slide scanner (VS200, Zeiss).

**STA-4783 Loading Efficiency and Release Curve.** To measure the loading efficiency of STA-4783, the drug-loaded SACCT NCs were completely disintegrated using hydrochloric acid. After centrifugation, the transparent supernatant was measured with HPLC (C18 chromatographic column, 254 nm) to calculate the STA-4783 content based on the standard curve. Besides, the time-dependent release curve of STA-4783 from SACCT NCs in different pH buffers (7.4, 6.0, and 5.0) followed a similar protocol to measure the released quantity.

**pH-Responsive Degradation Performance of SACCT NCs.** Different pH buffers (5.0, 6.0, 7.4) were prepared to mimic the metabolic environment during tumor treatment. 1 mg/mL SACCT NCs were suspended in the pH buffers and slightly oscillated at 37 °C. At time points of 1 and 24 h, SACCT NCs were collected and checked the structural changes were examined via TEM.

**POD-Like Catalytic Performance Measurement.** To evaluate the POD-like catalytic performance, 5,5-dimethyl-1-pyrroline *N*-oxide (DMPO) was employed as a free radical scavenger. 0.2 mL of $H_2O$, CT, ACCT, and SACCT NCs (200 $\mu$g/mL) was mixed with 0.1 mL of $H_2O_2$ (100 mM) and 10 $\mu$L of DMPO, respectively. The mixture was kept for 5 min and then measured by electron spin resonance (ESR, Bruker) to detect the free radicals.

Additionally, a TMB single-component solution was employed to assess POD-like catalytic performance. 0.1 mL of TMB solution, 0.3 mL of 50 mM $H_2O_2$ solution, and 0.5 mL of acetate buffer (pH 4) were mixed. Then, various NPs ($H_2O$, CT, ACCT, and SACCT NCs) at concentrations of 75, 150, 300, and 600 $\mu$g/mL were added, respectively. The mixture was kept in a 37 °C incubator for 30 min. Finally, the absorbance of oxidized TMB at 652 nm revealed the generated amount of ROS by the Fenton-like reaction of NPs.

**Cell Culture and *In Vitro* Cytotoxicity.** The mouse fibroblast cell line (L929), human osteosarcoma cell line (MG63), and mouse osteosarcoma osteoblast cell line (K7M2) were purchased from Wuhan Pricella Biotechnology Co., Ltd. and cultured according to standard protocols. Cells were cultured in a 96-well plate at a concentration of 5,000 cells/well in an incubator. 24 h later, the medium was replaced with a medium containing a gradient concentration of CT, ACCT, and SACCT NCs (0−1000 $\mu$g/mL). After another 24 h of incubation, the cell survival was measured by the CCK-8 assay (quantitatively) and Calcein-AM/PI staining (qualitatively). The half-maximal inhibitory concentration ($IC_{50}$) was calculated using GraphPad Prism.

**Cellular Uptake.** SACCT NCs were labeled using Coumarin-6 via absorption. K7M2 cells were seeded in confocal plates at a concentration of 1000 cells/well. 24 h later, the medium was replaced by a medium containing 15 $\mu$g/mL of Coumarin-6-labeled SACCT NCs. After 1 and 4 h of incubation, additional nanoparticles were washed away, and all cells were stained with DAPI and TRITC-Phalloidin to label the nucleus and cytoskeleton. Finally, fluorescence images were obtained by LSCM.

**Apoptosis and Necrosis Analysis.** K7M2 cells were cultured in a 6-well plate at a concentration of 10,000 cells/well in an incubator. 24 h later, the medium was replaced by 15 $\mu$g/mL of PBS, CT NPs, ACCT NCs, and SACCT NCs medium. After another 24 h of incubation, all cells were collected, washed with PBS, stained with an Annexin-V FITC/PI apoptosis detection kit, and finally analyzed by flow cytometry.

**Intracellular ROS Detection.** K7M2 cells were cultured in a 96-well plate at a concentration of 3,000 cells/well in an incubator. 24 h later, the medium was replaced by a medium containing 15 $\mu$g/mL of PBS, CT NPs, ACCT NCs, and SACCT NCs medium. After another 8 h of incubation, cells were washed with PBS, stained with a DCFH-DA probe, and finally imaged by LSCM.

**Mitochondrial Membrane Potential Detection by JC-1 Probes.** K7M2 cells were seeded in confocal plates at a concentration of 1000 cells/well. 24 h later, the cells were incubated with 15 $\mu$g/mL of PBS, CT NPs, ACCT NCs, and SACCT NCs medium for another 24 h. Cells were washed with PBS and stained with JC-1 working liquid, according to the standard protocol. Finally, fluorescence images were obtained by LSCM (Ex/Em = 490 nm/530 nm for JC-1 monomer, Ex/Em = 525 nm/590 nm for JC-1 aggregate).

**mRNA Extraction and Sequencing.** K7M2 cells ($1 \times 10^6$) were treated with 15 $\mu$g/mL PBS, CT NPs, ACCT NCs, and SACCT NCs medium for 24 h, respectively. Then, RNA was extracted using TRIzol reagent. RNA purity was measured using NanoDrop, and RNA integrity was assessed using the RNA Nano 6000 Assay Kit of the Agilent Bioanalyzer 2100 system. mRNA sequencing was conducted by ANOROAD GENOME (Beijing) Co. Ltd. to investigate the global expression profiles of differently treated K7M2 cells. The differentially expressed genes were analyzed using R and DESeq 2 package by the cutoff of log fold change >1 and *P* adjusted value of <0.05. Functional annotation and enrichment analysis of the significantly differentially expressed genes were analyzed using R and clusterProfiler package.

**Animal Care and Evaluation of *In Vivo* Antitumor Efficacy.** All animal experiments were carried out according to the guidelines and protocol (20231087) approved by the Animal Ethics Committee of The Second Xiangya Hospital, Central South University. Balb/c mice (6−8 weeks old) were brought from Beijing Vital River Laboratory Animal Technology Co., Ltd. and subcutaneously injected with K7M2 cells ($1 \times 10^7$) to build the model of K7M2-tumor-bearing mice. Once the tumor volume reached 100 $mm^3$, mice were randomly divided into five groups: (G1) PBS, (G2) STA-4783, (G3) CT NPs, (G4) ACCT NCs, and (G5) SACCT NCs. The nanoparticle formulation (100 $\mu$L, 10 mg/kg in PBS) was injected intravenously on days 0, 3, 6, 9, and 12 for a total of five times. Tumor volume and body weight of the mice were recorded every 5 days. Mouse survival rates were recorded for 2 months. After euthanasia, the main organs (heart, liver, spleen, lung, kidney, tumor) were collected for H&E staining and immunohistochemical analysis ($K_i$-67). Immunofluorescence analysis (c-Cas-1, LDHA, CRT, CD8, NLRP3, DLAT, FDX1,


https://doi.org/10.1021/acsnano.5c08243
ACS Nano XXXX, XXX, XXX−XXX

IFN-$\gamma$, IL-1$\beta$) was carried to identify the immune response caused by SACCT NCs treatment.

**ELISA for Cytokine Detection.** Cytokines in serum after different treatments (PBS, CT NPs, ACCT NCs, and SACCT NCs) were measured with ELISA kits according to the standard protocol, including IL-6 and TNF-$\alpha$. Besides, IL12, Il-10, and TGF-$\beta$ in tumor tissues after different treatments (PBS, CT NPs, ACCT NCs, and SACCT NCs) were measured by ELISA kits according to the standard protocol.

**Flow Cytometry Analysis.** Cells were stained with different panels of antibodies according to the vendor's protocols. To analyze DCs, CD45-APC-cy7, CD11b-FITC, CD80-BV421, CD86-PE, and CD11c-PE-Dazzle594 mouse mAbs were used to label cells. To analyze MDSCs, CD45-APC-cy7, CD11b-FITC, and Gr-1-BV650 mouse mAbs were used to label cells. To analyze activated T cells, CD45-APC-cy7, CD11b-FITC, CD3-PE-cy5, CD8-AlexaFlour 700, and CD4-Percp-cy5.5 mouse mAbs were employed to label cells. To analyze macrophages, CD45-APC-cy7, CD11b-FITC, F4/80-PE-cy7, and CD206-AlexaFlour 647 mouse mAbs were used to label the cells. All analyses were measured on BD FACS Aria Fusion Flow Cytometers.

**Data Statistical Analysis.** Statistical analysis was performed using GraphPad Prism (GraphPad Software, USA). Quantitative data were expressed as the mean ± standard deviation (SD). Statistically significant differences ($p$) were analyzed by Student's $t$-test or one-way ANOVA with a Tukey test. **** $p < 0.0001$, *** $p < 0.001$, ** $p < 0.01$, * $p < 0.05$, ns $p > 0.05$.

## ASSOCIATED CONTENT

### Supporting Information

The Supporting Information is available free of charge at https://pubs.acs.org/doi/10.1021/acsnano.5c08243.

Figure S1: the TEM images of CT NPs and $Cu_2O$ NCs; Figure S2: Calcein-AM (living) and PI (dead) staining of K7M2 cells after different treatments; Figure S3: mitochondrial membrane potential detection by JC-1 probe staining of K7M2 cells after different treatments; Figure S4: transcription analysis of K7M2 cells by RNA-seq upon various treatments; Figure S5: quantification of total fluorescence intensity at the tumor site at different time points after SACCT NCs injection; Figure S6: the assessment of main organs (heart, liver, spleen, lung, and kidney) function by H&E staining in various treatment groups; Figure S7: biosafety evaluation of SACCT NCs *in vivo* via biochemical analysis of whole blood; Figure S8: biosafety evaluation of SACCT NCs *in vivo* via biochemical analysis of serum; Figure S9: gating strategies for FCM analysis images of $CD8^+$T cells ($CD45^+CD11b^-CD3^+CD8^+$) within tumor tissues after various treatments; Figure S10: gating strategies of $CD8^+$ T cells ($CD45^+CD3^+CD8^+$) within the spleen after various treatments; Figure S11: IFN-$\gamma$ and IL-1$\beta$ expression within tumor tissues after various treatments; Figure S12: gating strategies for FCM analysis images of mature DCs ($CD45^+CD11b^+CD11c^+CD80^+CD86^+$) within tumor tissues after various treatments; Figure S13: gating strategies and representative FCM analysis images of mature DCs ($CD45^+CD11b^+CD80^+CD86^+$) within TDLNs after various treatments; Figure S14: gating strategies and representative FCM analysis images of M1 macrophages ($CD45^+CD11b^+F4/80^+CD80^+$) within tumor tissues after various treatments; Figure S15. Gating strategies and representative FCM analysis images of M2 macrophages ($CD45^+CD11b^+F4/80^+CD206^+$) within tumor tissues after various treatments; Figure S16: the percentage of M1 macrophages and M2 macrophages within tumor tissues after various treatments; Figure S17: the amount of cytokines IL-12, IL-10, and TGF-$\beta$ in tumor tissues after various treatments; Figure S18: gating strategies and representative FCM analysis images of MDSCs ($CD45^+CD11b^+Gr-1^+$) within tumor tissues after various treatments (PDF)

## AUTHOR INFORMATION


### Corresponding Authors

**Xing Wang** − *State Key Laboratory of Organic−Inorganic Composites, College of Life Science and Technology, Beijing University of Chemical Technology, Beijing 100029, P. R. China;* orcid.org/0000-0002-9990-1479; Email: wangxing@mail.buct.edu.cn

**Wensheng Xie** − *State Key Laboratory of Organic−Inorganic Composites, College of Life Science and Technology, Beijing University of Chemical Technology, Beijing 100029, P. R. China;* orcid.org/0000-0001-7700-9626; Email: xws@mail.buct.edu.cn

**Guanghui Zhu** − *The Affiliated Children's Hospital of Xiangya School of Medicine, Hunan Provincial Key Laboratory of Pediatric Orthopedics, Central South University (Hunan Children's Hospital), Changsha, Hunan 410007, P. R. China;* Email: zgh5650@163.com

### Authors

**Guangyao Jiang** − *State Key Laboratory of Organic−Inorganic Composites, College of Life Science and Technology, Beijing University of Chemical Technology, Beijing 100029, P. R. China; Department of Orthopedics, The Second Xiangya Hospital, Central South University, Changsha, Hunan 410011, P. R. China*

**Fangming Zhang** − *State Key Laboratory of Organic−Inorganic Composites, College of Life Science and Technology, Beijing University of Chemical Technology, Beijing 100029, P. R. China*

**Ziyi Wu** − *Department of Orthopedics, The Second Xiangya Hospital, Central South University, Changsha, Hunan 410011, P. R. China*

**Xianghong Zhang** − *Department of Orthopedics, The Second Xiangya Hospital, Central South University, Changsha, Hunan 410011, P. R. China*

**Jingxia Xu** − *State Key Laboratory of Organic−Inorganic Composites, College of Life Science and Technology, Beijing University of Chemical Technology, Beijing 100029, P. R. China*

**Zhuyuan Peng** − *State Key Laboratory of Organic−Inorganic Composites, College of Life Science and Technology, Beijing University of Chemical Technology, Beijing 100029, P. R. China*

**Guofeng Li** − *State Key Laboratory of Organic−Inorganic Composites, College of Life Science and Technology, Beijing University of Chemical Technology, Beijing 100029, P. R. China;* orcid.org/0000-0002-4101-0059

Complete contact information is available at: https://pubs.acs.org/10.1021/acsnano.5c08243




https://doi.org/10.1021/acsnano.5c08243
ACS Nano XXXX, XXX, XXX−XXX

## Notes

The authors declare no competing financial interest.

## ACKNOWLEDGMENTS

G. Jiang, F. Zhang, and Z. Wu contributed equally to this study. This work was supported by the Natural Science Foundation of Beijing Municipality (2254093), the Project of Science and Technology of Yinchuan (2024SFZD004), and the National Natural Science Foundation of China (22275013). Many thanks for the funding support from the Peking University Third Hospital Fund for Interdisciplinary Research (PT2517, BYSYJC2024036) and the Fundamental Research Funds for the Central Universities (buctrc202419).

## REFERENCES

(1) Beird, H. C.; Bielack, S. S.; Flanagan, A. M.; Gill, J.; Heymann, D.; Janeway, K. A.; Livingston, J. A.; Roberts, R. D.; Strauss, S. J.; Gorlick, R. Osteosarcoma. *Nat. Rev. Dis. Primers* **2022**, *8* (1), 77.

(2) Kansara, M.; Teng, M. W.; Smyth, M. J.; Thomas, D. M. Translational Biology of Osteosarcoma. *Nat. Rev. Cancer* **2014**, *14* (11), 722−735.

(3) Gill, J.; Gorlick, R. Advancing Therapy for Osteosarcoma. *Nat. Rev. Clin. Oncol* **2021**, *18* (10), 609−624.

(4) Meltzer, P. S.; Helman, L. J. New Horizons in the Treatment of Osteosarcoma. *N. Engl. J. Med* **2021**, *385* (22), 2066−2076.

(5) Thanindratarn, P.; Dean, D. C.; Nelson, S. D.; Hornicek, F. J.; Duan, Z. Advances in Immune Checkpoint Inhibitors for Bone Sarcoma Therapy. *J. Bone Oncol* **2019**, *15*, 100221.

(6) Yi, Y.; Yu, M.; Feng, C.; Hao, H.; Zeng, W.; Lin, C.; Chen, H.; Lv, F.; Zhu, D.; Ji, X.; Mei, L.; Wu, M.; Tao, W. Transforming "Cold" Tumors into "Hot" Ones via Tumor-Microenvironment-Responsive siRNA Micelleplexes for Enhanced Immunotherapy. *Matter* **2022**, *5* (7), 2285−2305.

(7) Chen, T.; Zeng, W.; Tie, C.; Yu, M.; Hao, H.; Deng, Y.; Li, Q.; Zheng, H.; Wu, M.; Mei, L. Engineered Gold/Black Phosphorus Nanoplatforms with Remodeling Tumor Microenvironment for Sonoactivated Catalytic Tumor Theranostics. *Bioact. Mater* **2022**, *10*, 515−525.

(8) Zhang, F.; Zhang, Z.; Yang, W.; Peng, Z.; Sun, J.; Li, G.; Wei, Y.; Wang, X.; Zhao, L.; Xie, W. Engineering Autologous Cell-Derived Exosomes to Boost Melanoma-Targeted Radio-Immunotherapy by Cascade cGAS-STING Pathway Activation. *Small* **2025**, *21* (4), 2408769.

(9) Chen, C.; Xie, L.; Ren, T.; Huang, Y.; Xu, J.; Guo, W. Immunotherapy for Osteosarcoma: Fundamental Mechanism, Rationale, and Recent Breakthroughs. *Cancer Lett* **2021**, *500*, 1−10.

(10) Huang, X.; Wang, L.; Guo, H.; Zhang, W. Single-Cell RNA Sequencing Reveals SERPINE1-Expressing CAFs Remodelling Tumour Microenvironment in Recurrent Osteosarcoma. *Clin. Transl. Med* **2024**, *14* (1), No. e1527.

(11) Fujiwara, T.; Yakoub, M. A.; Chandler, A.; Christ, A. B.; Yang, G.; Ouerfelli, O.; Rajasekhar, V. K.; Yoshida, A.; Kondo, H.; Hata, T.; Tazawa, H.; Dogan, Y.; Moore, M. A. S.; Fujiwara, T.; Ozaki, T.; Purdue, E.; Healey, J. H. CSF1/CSF1R Signaling Inhibitor Pexidartinib (PLX3397) Reprograms Tumor-Associated Macrophages and Stimulates T-Cell Infiltration in the Sarcoma Microenvironment. *Mol. Cancer Ther* **2021**, *20* (8), 1388−1399.

(12) Wang, Z.; Liu, S.; Ming, R.; Wang, W.; Wang, C.; Li, C.; Yang, J.; Zhang, F.; Lu, G.; Mei, L.; Huang, L.-L. Engineered Virus-Mimicking Nanovaccine with Lymph Node−Tumor Dual-Targeting and STING-Activating Capacity for Robust Cancer Immunotherapy. *J. Controlled Release* **2025**, *378*, 416−427.

(13) Li, H.; Li, Y.; Su, L.; Zheng, K.; Zhang, Y.; Li, J.; Lv, F.; Huang, M.; Chen, T.; Zhang, H.; Shi, Z.; Zhu, D.; Dong, X.; Zeng, W.; Mei, L. Enzyme-empowered "Two Birds with One Stone" Strategy for Amplifying Tumor Apoptosis and Metabolic Clearance. *Adv. Sci* **2024**, *11* (18), 2308251.

(14) Kager, L.; Pötschger, U.; Bielack, S. Review of Mifamurtide in the Treatment of Patients with Osteosarcoma. *Ther. Clin. Risk Manage.* **2010**, *6*, 279.

(15) Wen, Y.; Tang, F.; Tu, C.; Hornicek, F.; Duan, Z.; Min, L. Immune Checkpoints in Osteosarcoma: Recent Advances and Therapeutic Potential. *Cancer Lett* **2022**, *547*, 215887.

(16) Galon, J.; Bruni, D. Approaches to Treat Immune Hot, Altered and Cold Tumours with Combination Immunotherapies. *Nat. Rev. Drug Discovery* **2019**, *18* (3), 197−218.

(17) Duan, Q.; Zhang, H.; Zheng, J.; Zhang, L. Turning Cold into Hot: Firing up the Tumor Microenvironment. *Trends Cancer* **2020**, *6* (7), 605−618.

(18) Galluzzi, L.; Guilbaud, E.; Schmidt, D.; Kroemer, G.; Marincola, F. M. Targeting Immunogenic Cell Stress and Death for Cancer Therapy. *Nat. Rev. Drug Discovery* **2024**, *23* (6), 445−460.

(19) Roerden, M.; Spranger, S. Cancer Immune Evasion, Immunoediting and Intratumour Heterogeneity. *Nat. Rev. Immunol* **2025**, *25*, 353−369.

(20) Zhang, H.; Zhang, Y.; Zhang, Y.; Li, H.; Ou, M.; Yu, Y.; Zhang, F.; Yin, H.; Mao, Z.; Mei, L. Catalytic Activity of Violet Phosphorus-Based Nanosystems and the Role of Metabolites in Tumor Therapy. *Nat. Commun* **2024**, *15* (1), 6783.

(21) Wang, J.; Zhang, Y.; Jia, Y.; Xing, H.; Xu, F.; Xia, B.; Lai, W.; Yuan, Y.; Li, X.; Shan, S.; Chen, J.; Guo, W.; Zhang, J.; Zheng, A.; Li, J.; Gong, N.; Liang, X.-J. Targeting Vaccines to Dendritic Cells by Mimicking the Processing and Presentation of Antigens in Xenotransplant Rejection. *Nat. Biomed. Eng* **2025**, *9* (2), 201−214.

(22) Xie, W.; Ye, J.; Guo, Z.; Lu, J.; Xu, W.; Gao, X.; Huang, H.; Hu, R.; Mao, L.; Wei, Y.; Zhao, L. TME-Responded Full-Biodegradable Nanocatalyst for Mitochondrial Calcium Overload-Induced Hydroxyl Radical Bursting Cancer Treatment. *Chem. Eng. J* **2022**, *438*, 135372.

(23) Xie, W.; Guo, Z.; Zhao, L.; Wei, Y. Metal-Phenolic Networks: Facile Assembled Complexes for Cancer Theranostics. *Theranostics* **2021**, *11* (13), 6407−6426.

(24) Xie, W.; Guo, Z.; Zhao, L.; Wei, Y. The Copper Age in Cancer Treatment: From Copper Metabolism to Cuproptosis. *Prog. Mater. Sci* **2023**, *138*, 101145.

(25) Tang, Z.; Zhao, P.; Wang, H.; Liu, Y.; Bu, W. Biomedicine Meets Fenton Chemistry. *Chem. Rev* **2021**, *121* (4), 1981−2019.

(26) Xie, W.; Zhang, G.; Guo, Z.; Lu, J.; Ye, J.; Xu, W.; Gao, X.; Yue, K.; Wei, Y.; Zhao, L. Ultra-Sensitive Iron-Doped Palladium Nanocrystals with Enhanced Hydroxyl Radical Generation for Chemo-/Chemodynamic Nanotherapy. *Adv. Funct. Mater* **2022**, *32* (12), 2107518.

(27) Palma, F. R.; Gantner, B. N.; Sakiyama, M. J.; Kayzuka, C.; Shukla, S.; Lacchini, R.; Cunniff, B.; Bonini, M. G. ROS Production by Mitochondria: Function or Dysfunction? *Oncogene* **2024**, *43* (5), 295−303.

(28) Wang, X.; Sun, B.; Dai, Q.; Zhu, L.; Gu, Z.; Dai, L. Metal-Free Carbon Co-Catalysts for up-Conversion Photo-Induced Catalytic Cancer Therapy. *Adv. Mater* **2024**, *36* (42), 2408560.

(29) Guo, Z.; Gao, X.; Lu, J.; Li, Y.; Jin, Z.; Fahad, A.; Pambe, N. U.; Ejima, H.; Sun, X.; Wang, X.; Xie, W.; Zhang, G.; Zhao, L. Apoptosis and Paraptosis Induced by Disulfiram-Loaded Ca2+/Cu2+ Dual-Ions Nano Trap for Breast Cancer Treatment. *ACS Nano* **2024**, *18* (9), 6975−6989.

(30) Tsvetkov, P.; Coy, S.; Petrova, B.; Dreishpoon, M.; Verma, A.; Abdusamad, M.; Rossen, J.; Joesch-Cohen, L.; Humeidi, R.; Spangler, R. D.; Eaton, J. K.; Frenkel, E.; Kocak, M.; Corsello, S. M.; Lutsenko, S.; Kanarek, N.; Santagata, S.; Golub, T. R. Copper Induces Cell Death by Targeting Lipoylated TCA Cycle Proteins. *Science* **2022**, *375* (6586), 1254−1261.

(31) Tang, D.; Chen, X.; Kroemer, G. Cuproptosis: A Copper-Triggered Modality of Mitochondrial Cell Death. *Cell Res* **2022**, *32* (5), 417−418.

(32) Wang, W.; Mo, W.; Hang, Z.; Huang, Y.; Yi, H.; Sun, Z.; Lei, A. Cuproptosis: Harnessing Transition Metal for Cancer Therapy. *ACS Nano* **2023**, *17* (20), 19581−19599.



https://doi.org/10.1021/acsnano.5c08243
*ACS Nano* XXXX, XXX, XXX−XXX

(33) Guo, B.; Yang, F.; Zhang, L.; Zhao, Q.; Wang, W.; Yin, L.; Chen, D.; Wang, M.; Han, S.; Xiao, H.; Xing, N. Cuproptosis Induced by ROS Responsive Nanoparticles with Elesclomol and Copper Combined with αPD-L1 for Enhanced Cancer Immunotherapy. *Adv. Mater* **2023**, *35*, 2212267.
(34) Liu, H. Pan-Cancer Profiles of the Cuproptosis Gene Set. *Am. J. Cancer Res* **2022**, *12* (8), 4074−4081.
(35) Li, J.; Wu, F.; Li, C.; Sun, S.; Feng, C.; Wu, H.; Chen, X.; Wang, W.; Zhang, Y.; Liu, M.; et al. The Cuproptosis-Related Signature Predicts Prognosis and Indicates Immune Microenvironment in Breast Cancer. *Front. Genet* **2022**, *13*, 977322.
(36) Zhao, F.; Liang, L.; Wang, H.; Wang, C.; Su, D.; Ying, Y.; Li, W.; Li, J.; Zheng, J.; Qiao, L.; et al. $H_2S$-activated Ion-interference Therapy: A Novel Tumor Targeted Therapy Based on Copper-overload-mediated Cuproptosis and Pyroptosis. *Adv. Funct. Mater* **2023**, *33* (38), 2300941.
(37) Qiu, Z.; Liu, Q.; Wang, L.; Xiong, Y.; Wu, J.; Wang, M.; Yan, X.; Deng, H. The Copper Transporter, SLC31A1, Transcriptionally Activated by ELF3, Imbalances Copper Homeostasis to Exacerbate Cisplatin-Induced Acute Kidney Injury through Mitochondrial Dysfunction. *Chem.-Biol. Interact* **2024**, *393*, 110943.
(38) Song, L.; Zeng, R.; Yang, K.; Liu, W.; Xu, Z.; Kang, F. The Biological Significance of Cuproptosis-Key Gene MTF1 in Pan-Cancer and Its Inhibitory Effects on ROS-Mediated Cell Death of Liver Hepatocellular Carcinoma. *Discovery Oncol* **2023**, *14* (1), 113.
(39) Chong, W.; Ren, H.; Chen, H.; Xu, K.; Zhu, X.; Liu, Y.; Sang, Y.; Li, H.; Liu, J.; Ye, C.; Shang, L.; Jing, C.; Li, L. Clinical Features and Molecular Landscape of Cuproptosis Signature-Related Molecular Subtype in Gastric Cancer. *Imeta* **2024**, *3* (3), No. e190.
(40) Yan, B.; Liu, C.; Li, H.; Wen, N.; Jiao, W.; Wang, S.; Zhang, Y.; Zhang, T.; Zhang, H.; Lv, Y.; Fan, H.; Liu, X. Reversal of HMGA1-Mediated Immunosuppression Synergizes with Immunogenic Magnetothermodynamic for Improved Hepatocellular Carcinoma Therapy. *ACS Nano* **2023**, *17* (10), 9209−9223.
(41) Zheng, P.; Zhou, C.; Lu, L.; Liu, B.; Ding, Y. Elesclomol: A Copper Ionophore Targeting Mitochondrial Metabolism for Cancer Therapy. *J. Exp. Clin. Cancer Res* **2022**, *41* (1), 271.
(42) Seif-Eddine, M.; Cobb, S. J.; Dang, Y.; Abdiaziz, K.; Bajada, M. A.; Reisner, E.; Roessler, M. M. Operando Film-Electrochemical EPR Spectroscopy Tracks Radical Intermediates in Surface-Immobilized Catalysts. *Nat. Chem* **2024**, *16* (6), 1015−1023.
(43) Wang, Q.; Liang, Q.; Dou, J.; Zhou, H.; Zeng, C.; Pan, H.; Shen, Y.; Li, Q.; Liu, Y.; Leong, D. T.; Jiang, W.; Wang, Y. Breaking through the Basement Membrane Barrier to Improve Nanotherapeutic Delivery to Tumours. *Nat. Nanotechnol* **2024**, *19* (1), 95−105.
(44) Shimbo, K.; Hsu, G. W.; Nguyen, H.; Mahrus, S.; Trinidad, J. C.; Burlingame, A. L.; Wells, J. A. Quantitative Profiling of Caspase-Cleaved Substrates Reveals Different Drug-Induced and Cell-Type Patterns in Apoptosis. *Proc. Natl. Acad. Sci. U. S. A* **2012**, *109* (31), 12432−12437.
(45) Khan, F.; Lin, Y.; Ali, H.; Pang, L.; Dunterman, M.; Hsu, W.-H.; Frenis, K.; Grant Rowe, R.; Wainwright, D. A.; McCortney, K.; Billingham, L. K.; Miska, J.; Horbinski, C.; Lesniak, M. S.; Chen, P. Lactate Dehydrogenase a Regulates Tumor-Macrophage Symbiosis to Promote Glioblastoma Progression. *Nat. Commun* **2024**, *15* (1), 1987.
(46) Huang, Y.; Jiang, W.; Zhou, R. DAMP Sensing and Sterile Inflammation: Intracellular, Intercellular and Inter-Organ Pathways. *Nat. Rev. Immunol* **2024**, *24* (10), 703−719.
(47) Sharma, B. R.; Kanneganti, T.-D. NLRP3 Inflammasome in Cancer and Metabolic Diseases. *Nat. Immunol* **2021**, *22* (5), 550−559.

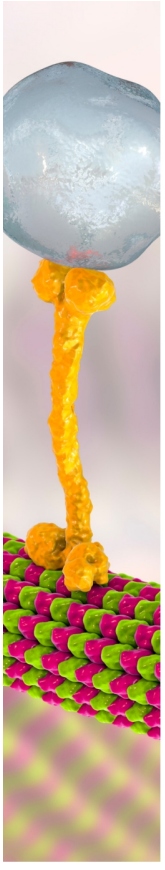





https://doi.org/10.1021/acsnano.5c08243
*ACS Nano* XXXX, XXX, XXX−XXX